Holocene stable isotope record of insolation and rapid climate change in a stalagmite from the Zagros of Iran

Andrews, J.E. [a,*] Carolin, S.A.[b,c], Peckover, E.N. [a], Marca, A. [a], Al-Omari, S[a,d] and Rowe, P.J. [a]

[a]School of Environmental Sciences, University of East Anglia, Norwich NR4 7TJ, UK.
[b]Department of Earth Sciences, University of Oxford, OX1 3AN Oxford, United Kingdom.
[c]Institute of Geology, University of Innsbruck, 6020 Innsbruck, Austria.
[d]Praxis, Office #1501, The Oberoi Center, Business Bay, P.O Box 413898 Dubai, UAE.

*Corresponding author email j.andrews@uea.ac.uk

Running header: Holocene stalagmite stable isotope climate record, Iran

Abstract

We explore Holocene climatic change as recorded by stable isotopes in a single, well-dated, stalagmite from the northern Zagros Mountains of Iran, a region where stalagmite records have so far only provided short glimpses of Holocene climatic changes. Stalagmite KT-3 from Katalekhor Cave began growing ~9.5 ka under wet early Holocene conditions ($\delta^{18}O$ values around or below -9.0‰, maximum growth diameter and lowest $^{234}U/^{238}U_0$ activity values). Progressive reduction in winter precipitation amount after 7.0 ka was driven by decreasing summer insolation, indicated by increasing $\delta^{18}O$ and $^{234}U/^{238}U_0$ activity values and reduction in growth diameter until ~2.0 ka. Centennial-scale variability is not a feature of the $\delta^{18}O$ record suggesting a stable winter recharge regime without marked interannual rainfall variability. KT-3 $\delta^{13}C$ compositions are enriched relative to lower altitude stalagmites in the Levant, implying low soil CO_2 contribution (thin montane soils) with stronger ingress of atmospheric CO_2. However, the $\delta^{13}C$ values also show ~ 1.5‰ centennial-scale variability with higher $\delta^{13}C$ values between 8.3-7.7 ka, 6.5-5.5 ka, 5.4-4.5 ka and ~4.3-2.0 ka: three of these correspond with Rapid Climate Change (RCC) events based on non-seasalt potassium (K^+) in Greenland ice cores. Higher $\delta^{13}C$ values indicate poor soil development caused by aridity. The first centennial-scale $\delta^{13}C$ anomaly (8.3-7.7 ka) is in part overprinted by the ~160 year-long, 8.2 ka cold/dry event, but culmination ~7.7 ka corresponds with other records suggesting an intensified Siberian High Pressure system affecting regional climate. The centennial-scale $\delta^{13}C$ anomaly between 4.3 and 2.0 ka overlaps the 2.65 to 2.50 ka 'Assyrian megadrought' evident in stalagmite stable isotope records in northern Iraq. The KT-3 record is key in better understanding Holocene climate change in the central Zagros region, representative of montane 'fertile crescent' environments. The KT-3 $\delta^{18}O$ record also suggests that nearby lacustrine carbonate isotope records (Lakes Zeribar and Mirabad) can be reinterpreted as insolation-driven records, starting wet, but with recharge decreasing until ~7.0 ka, followed broadly by developing aridity.

Key words: Holocene; paleoclimatology; Eastern Europe; stable isotopes; stalagmite; Iran; Zagros; rapid climate change.

1. Introduction

Holocene palaeoclimate records for the Middle East show clear heterogeneity linked to local delivery of precipitation that results from complex meteorological interactions (Burstyn et al. 2019). The region as a whole encompasses transitions between temperate Mediterranean (Mediterranean Levant) to more arid deserts in Levant rain shadow regions (Bar-Matthews et al., 2019), to sub-tropical deserts of the Arabian Peninsula, to semi-arid montane environments in the 'Fertile Crescent' between E. Turkey and NW Iran. Mediterranean cyclones deliver much of the regional precipitation in the Mediterranean Levant (Bar-Matthews et al., 2019). These are generated by interplay between local low pressure systems, major N. Atlantic synoptic systems and local cyclogenesis that can be heavily influenced on decadal to centennial timescales by outbreaks of cold northerly polar/continental (NPC) air (Rohling et al., 2019). The Fertile Crescent (FC), like the Levant, currently receives most of its precipitation during winter, from Mediterranean storm tracks (Ulbrich et al., 2012), but in the eastern FC also from cyclogenesis in the Arabian Sea, Persian Gulf, Red Sea, and north Indian ocean (Evans and Smith, 2006).

While our understanding of modern meteorological conditions in the FC is developing, this region has few Holocene (and older) speleothem-based proxy records, such that Burstyn et al. (2019) identify the region as a priority for future palaeoclimate research. $\delta^{18}O$ in stalagmite calcite largely records the winter-dominated precipitation with high resolution chronology potentially allowing identification of the relative regional influence of the Indian Summer Monsoon and the Siberian High, the latter probably implicated in Holocene Rapid Climate Change events (RCCs) that in montane settings may express as cold and dry events (Rohling et al., 2019). Stalagmite proxies should also complement and improve upon lake and pollen archives that largely record annual or summer-dominated precipitation/temperature changes (Burstyn et al., 2019). In fact Holocene FC palaeoclimate reconstruction has until recently been heavily influenced by geochemical, palynological and plant macrofossil data from Iranian Lakes Zeribar and Mirabad (Fig. 1; Stevens et al., 2001; 2006). Current interpretations of these lake proxies register contradictions that require better explanation.

Regional FC palaeoclimate archives wholly independent of pollen records are now available in NW Iran (Sharifi et al., 2015; Fig. 1), but so far, stalagmites from northern Iran and Iraq (Fig. 1) have provided only short glimpses of Holocene climate. These include apparently wet conditions between 7.5 and 6.5 ka (Mehterian et al., 2017) and largely drier climate between 5.2 and 3.7 ka (Carolin et al., 2019). After 3.0 ka there is evidence of centennial-scale pluvial and drought conditions in the Tigris regions of northern Iraq (Sinha et al., 2019) followed by largely dry conditions after 2.4 ka (Flohr et al., 2017). Stalagmites from Qal'e Kord Cave in central NW Iran (Mehterian et al., 2017; Fig. 1) have continuous $\delta^{18}O$ records between 127-73 ka, i.e., mainly during marine isotope stage (MIS) 5, that follow the solar insolation curve at 30ºN and capture Dansgaard/Oeschger stadial and interstadial events. This indicates a strong atmospheric teleconnection in MIS 5 between north Atlantic climate and central NW Iran, with maximum orbital configuration driving increased winter precipitation (Kutzbach et al., 2014).

A strong influence from solar insolation on Holocene (MIS 1) palaeoclimate in the region is inferred from sedimentary geochemical records at Neor peat mire (Sharifi et al., 2015; Fig. 1). Here, the data record the transition from a dry Younger Dryas (YD) to a much wetter early Holocene (9.0-6.0 ka) similar to the wet early Holocene conditions recorded in Mediterranean lake records (Roberts et al., 2008) and a speleothem from NW Turkey (Rowe et al., 2012; Fig. 1). At Neor mire, drier and dustier conditions established after 6.0 ka.

In this paper we discuss a new record from a stalagmite in Katalekhor Cave (Fig. 1) which grew through most of the Holocene. This new record allows better understanding of Holocene climate change in the central Zagros region (just east of the FC), its detailed relationship to forcing by solar insolation ($\delta^{18}O$ record) and the expression of RCCs in the $\delta^{13}C$ record. This enables more confident linkage between Holocene palaeoclimatic events in the central Zagros region with those in the eastern Mediterranean, and the monsoonal Arabian Sea region to the SE. Sited just 60 km W of Qal'e Kord Cave, the Katalekhor stalagmite also allows more complete linkage of regional climate changes during the two most recent inter-glaciations. At regional scale the Katalekhor stalagmite also presents an opportunity to deconvolve contradictions in the Zeribar/Mirabad records (situated 180 km W and 300 km SSW of Katalekhor Cave respectively) enhancing the utility of these long established lacustrine palaeoclimate archives.

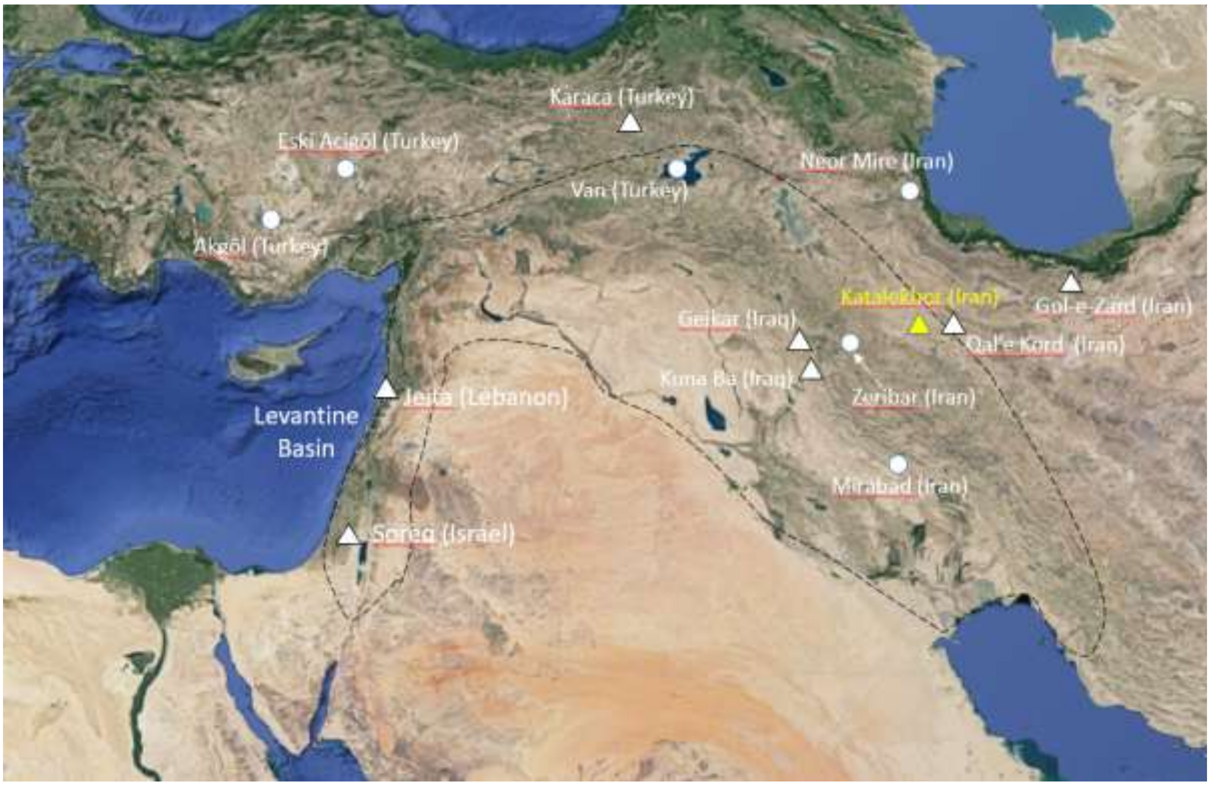

Fig. 1. Map of Middle East showing location of Katalekhor Cave, and other cave (triangles) or lake (dots) sites discussed in the text that contain important Holocene palaeoclimate records. The dashed lines marks the approximate boundary of the Fertile Crescent. Base image courtesy of Google Maps.

2. Cave environmental setting

Katalekhor Cave (35º 50.7' 2.02" N, 048º 09' 38.61" E; Fig. 1) is located in Zanjan Province ~300 km west of Tehran. The cave is located in the Sanandaj-Sirjan structural sub-zone of the Zagros Fold and Trust Belts (Karimi Vardanjani et al., 2017). The cave entrance is at 1719 m elevation in a W-E oriented anticline formed of Oligocene-Miocene aged, partially dolomitised limestone of the Qom Formation (Sardarabadi et al., 2016; Karimi Vardanjani et al., 2017), an inlier within surrounding conglomerates, sandstones and limestones of Pliocene age. To the SE the Qom Formation contains gypsum bearing-marls and red beds are present both below (Lower Red Formation; Oligocene) and above (Upper Red Formation: Miocene) the Qom Formation (Berberian 1974; Karevan et al., 2014), the latter including sandstones, marls and conglomerates with minor gypsum.

There is no record of Quaternary glacial geomorphology in the vicinity of the cave (see e.g. Ebrahimi and Seif 2016), although present day mean winter temperatures ~0 ºC are low enough to infer that periglacial conditions would have affected the regolith during the coldest phases of glacial periods. Further south at Zardkuh mean annual temperatures during the last glacial maximum (LGM) were ~9.7 ºC lower than present day (Ebrahimi and Seif 2016), suggesting Katalekhor LGM mean annual temperatures ~6 ºC with much colder winters.

Surface karst landforms are not developed in the region (Karimi Vardanjani et al., 2017) but beyond 200 m within the cave the subsurface epikarst is >200 m thick (based on the schematic section of Ahmadzade and Elmizadeh 2014). The site is at about upper treeline altitude, which is probably controlled by winter temperature rather than moisture deficit (Wright 1962), explaining the poor present day soil cover with patchy alpine grass vegetation.

The natural cave entrance was a ~1 m diameter crawl space, widened in the 1990s when the cave was developed for public access. The cave has been surveyed over 20,000 m on three levels (Arshadi and Laumanns 2004; Karimi Vardanjani et al., 2017) and contains a number of galleries with standing water pools during the winter months. Relative humidity in the second gallery of the upper level (~750 m from the cave entrance) at the site of sample collection in November 2006 was 100% with spot temperatures between 15.5 ºC - 16.6 ºC.

2.1. Modern climate and groundwater

The eastern forelands of the Zagros Mountains in the region of Katalekhor Cave have a climatic regime of hot, dry summers and cool wet winters. The annual precipitation is 300 - 400 mm (Fig. 2; Dinpashoh et al., 2004; Modarres and Sarhadi 2011; Khalili and Rahimi,

2014) of which >90% falls during the wet season from October to May, with a maximum in spring (March to May) (Fig. 3; Fallah et al., 2015; Raziei et al., 2014). During summer, descending anticyclonic air over the Iranian Plateau, promotes very stable, dry conditions although occasional summer rainfall (~10 mm) may be generated by convective and/or topographic mechanisms (Raziei et al., 2012), as vapour transport is deflected along the western foothills by warm winds from the Central Iranian Plateau (Evans et al., 2004; Stevens et al., 2001). Groundwater recharge thus occurs predominantly between October and April and while winter temperatures at the cave site are unlikely to significantly affect soil infiltration by prolonged freezing, summer aridity (low rainfall/high evaporation) will severely limit recharge such that summer drip water supply to speleothems will be highly dependent on epikarst storage capacity.

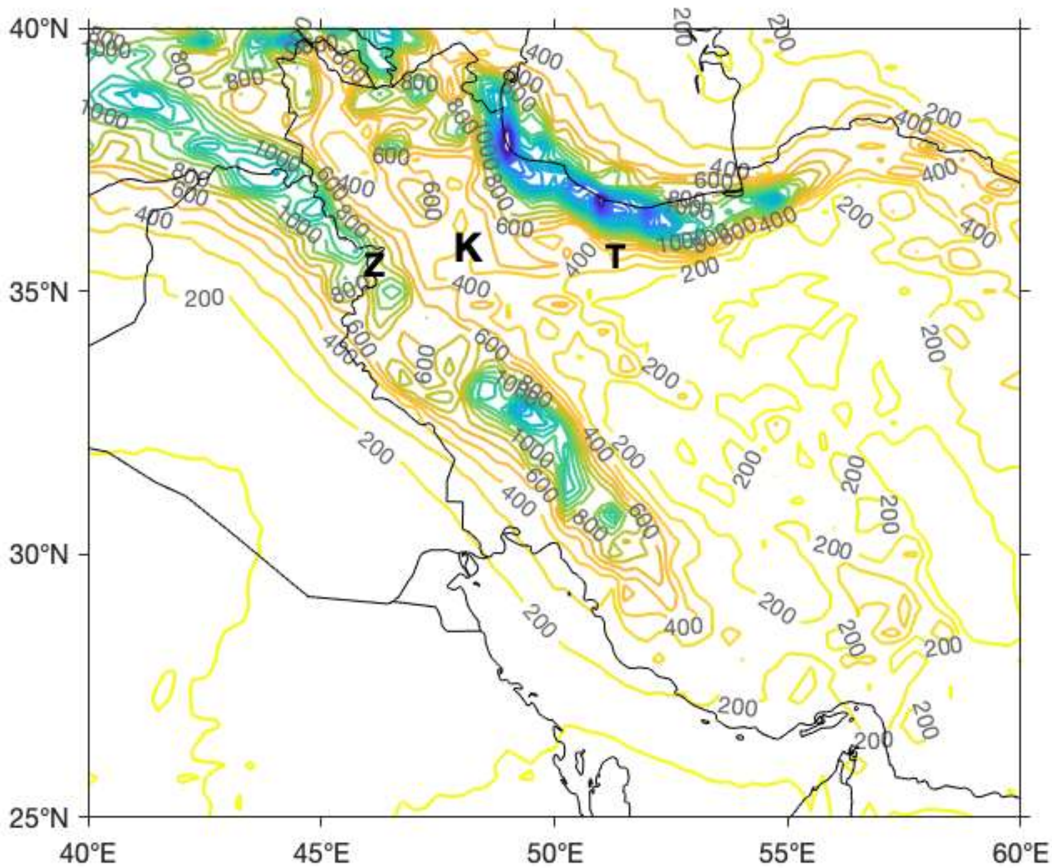

Fig. 2. Regional map showing contours of average annual precipitation between 1979 and 2018 (C3S, 2017). Data generated using Copernicus Climate Change Service Information 2019. K is location of Katalekhor Cave, T is location of Tehran and Z is the location of Lake Zeribar.

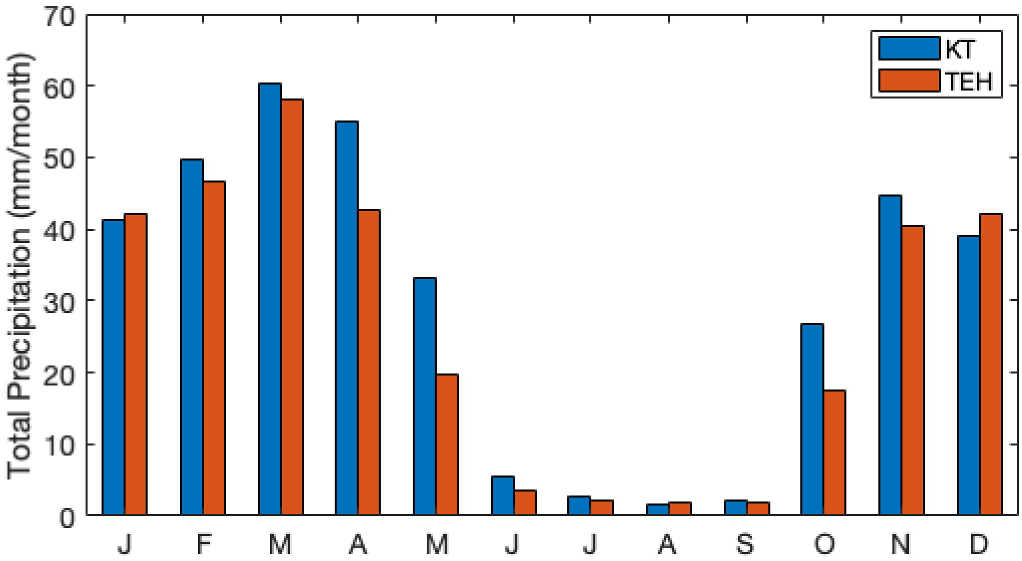

Fig. 3. Long-term monthly average precipitation for Tehran and Katalekhor Cave (C3S, 2017). Reanalysis precipitation data closest to each site is averaged over a 0.25º x 0.25º grid (~625 km2). Data generated using Copernicus Climate Change Service Information 2019.

Winter-spring rainfall in northwest Iran is associated with incursions of Mediterranean and polar maritime air masses, the latter ultimately deriving from the North Atlantic, that cross the Zagros Mountains from the west and north-west. Within these air masses, mid-tropospheric troughs commonly form upstream of Iran, over the eastern Mediterranean or Syria and Jordan (Evans and Smith 2006; Raziei et al., 2012, 2013). The combination of low pressure to the west and a semi-permanent Arabian anticyclone over the Arabian Sea to the southeast, results in strong moisture transport north and north-east from the Eastern Mediterranean, Red Sea, Persian Gulf and Arabian Sea (Evans and Smith 2006; Raziei et al., 2012, 2013). Subsequent orographic uplift over the western Zagros leads to heavy precipitation, some of which crosses the mountains into northwest Iran. A back-trajectory study of 900 precipitation events in Iran from 2010 - 2016 (Heydarizad et al., 2019) shows Katalekhor situated in a zone where polar maritime, Mediterranean and the southern marine water bodies are the dominant moisture sources, the influence of the Caspian Sea being limited by the Alborz Mountains.

3. Materials and methods

Stalagmite KT-3 is 567 mm long (Fig. 4) and was under an active drip when collected in November 2006. It comes from the second gallery of the upper level ~750 m from the cave entrance. U/Th dates show that growth of KT-3 initiated during the last interglacial period (Fig. 4) but this paper focusses on the upper 304 mm of Holocene growth.

U/Th samples were drilled from a slab of KT-3 along individual laminas at various distances from the base of the stalagmite (Fig. 4). Samples were drilled a few mm off the central growth axis using a 0.8 mm diameter tungsten carbide drill bit attached to a handheld dental drill. Individual sample size ranged from 100-200 mg calcite, with uranium concentrations ranging from 200-700 ppb. The stalagmite was generally clean of detrital contaminants, with thorium concentration ranging from 0.08-0.4 ppb.

To measure their U and Th radiogenic isotope ratios, the U/Th age samples were dissolved in nitric acid and spiked with a mixed ^{229}Th-^{236}U solution (Robinson et al., 2004). The U and Th fractions were then separated following procedures adapted from Edwards et al. (1987). U and Th isotopes were measured using a Nu Plasma multi-collector inductively coupled plasma mass spectrometer (MC-ICP-MS) in the Earth Sciences Department at Oxford University, following the procedures described in Vaks et al. (2013). Individual ages and 95% confidence intervals were calculated using an Oxford in-house Monte Carlo script that incorporates chemical blank errors, analytical uncertainties, and an initial ^{230}Th/^{232}Th ratio uncertainty. An initial bulk earth (^{230}Th/^{232}Th) atomic ratio of 0.5-10.8 ppm (uniform distribution) was applied to calculate corrected ages from samples with detrital thorium contamination. The U and Th concentrations, radiogenic isotope ratios used in the age calculation, and calculated uncorrected and corrected ages with errors are provided in Table 1.

The age model with 68% and 95% confidence ranges was produced using OxCal Version 4.3 Poisson-process deposition model (k_0= 1 cm^{-1}, $\log_{10}(k/k_0)$ = U(-2,2)), with interpolation (Bronk Ramsey, 2008; Bronk Ramsey and Lee, 2013). The difference between the mean calculated ages and mean OxCal modeled ages is small, less than 5 years for all samples, as all calculated ages were in chronological order along the growth axis originally. A depth v. age plot of individual U/Th age samples and the interpolated age model with errors is provided in Figure 4.

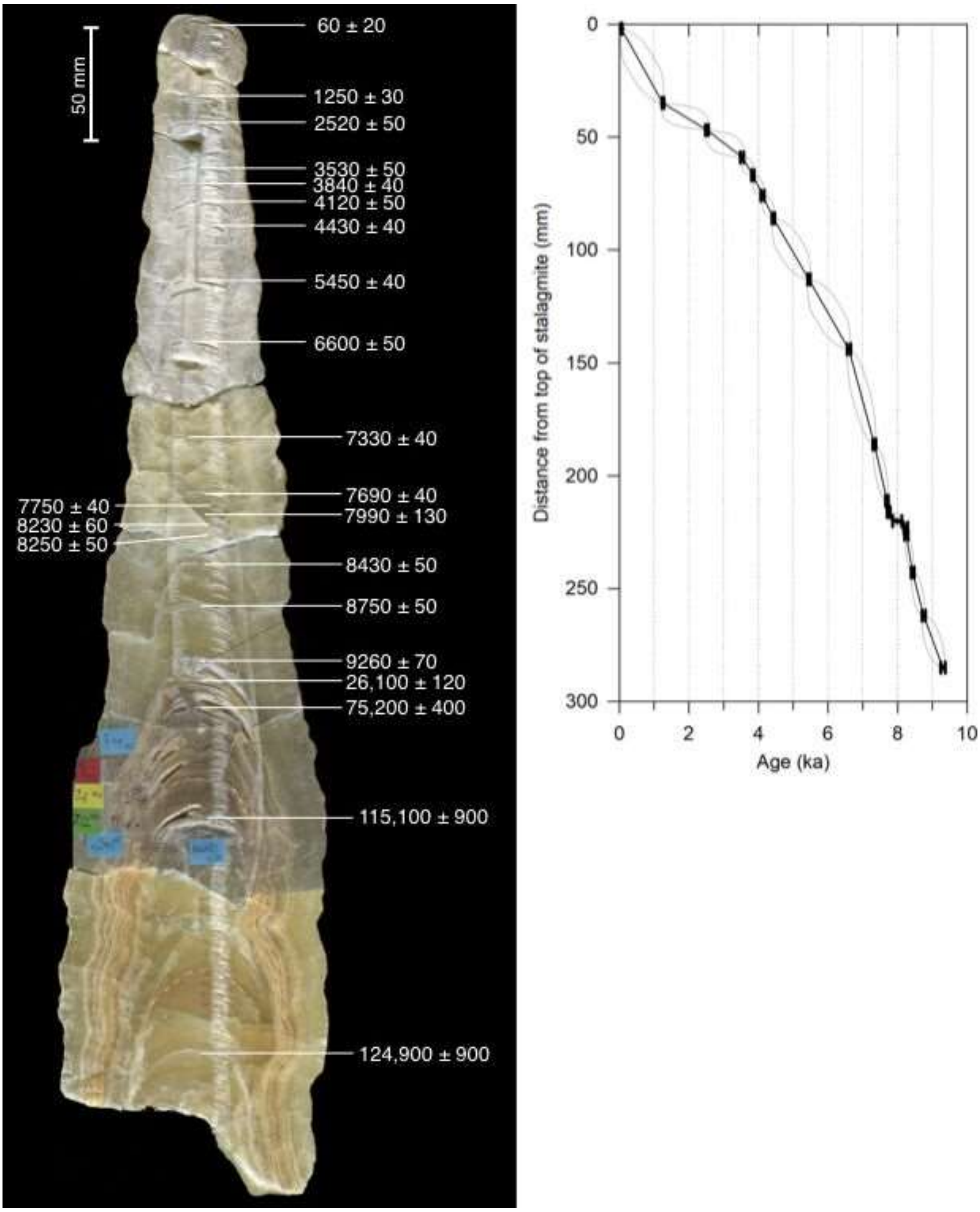

Fig. 4. Left panel shows an axial slab of KT-3 with U/Th sample positions and measured ages with 2sigma error. Right panel shows the Holocene U-Th age-depth model derived by OxCal v.4.3 from the data in Table 1 (solid black line). Upper and lower grey lines represent 95% confidence ranges produced by OxCal. Measured U/Th age 2sigma capped error bars are plotted in black bold. The model-adjusted mean ages are within a few years of the original mean ages (Table 1).

sample ID	Distance from stalagmite top (mm)	^{238}U conc (ppb)	^{232}Th (ppb)	(234/238) measured	(230/238) measured	(232/238) measured	Uncorr Age (yr)	Corr Age (yr)	Age (yr b1950)	+2s Error (yr)	-2s Error (yr)	(234/238) initial	Oxcal Model Age (yr b1950)
ag07	2	373	0.3	2.278 ± 0.007	0.0028 ± 0.0004	2.91e-04 ± 2e-06	140	120	60	20	20	2.278 ± 0.007	60
al01	35	309	0.3	2.446 ± 0.008	0.0295 ± 0.0005	1.54e-04 ± 3e-06	1320	1310	1250	30	20	2.451 ± 0.008	1250
aq07	47	185	0.1	2.461 ± 0.010	0.0580 ± 0.0009	1.77e-04 ± 6e-06	2600	2590	2520	40	50	2.471 ± 0.009	2520
aq08	59	216	0.1	2.473 ± 0.010	0.0808 ± 0.0011	1.89e-04 ± 6e-06	3610	3600	3530	50	50	2.487 ± 0.009	3530
aq02	67	281	0.1	2.373 ± 0.009	0.0840 ± 0.0008	1.47e-04 ± 4e-06	3920	3910	3840	40	40	2.388 ± 0.009	3840
ag06	76	269	0.1	2.361 ± 0.007	0.0897 ± 0.0009	5.14e-04 ± 4e-06	4210	4190	4120	50	50	2.377 ± 0.007	4120
al02	86	248	0.1	2.342 ± 0.008	0.0952 ± 0.0008	3.37e-04 ± 4e-06	4510	4490	4430	40	40	2.359 ± 0.008	4430
al03	113	301	0.1	2.255 ± 0.007	0.1119 ± 0.0009	1.54e-04 ± 4e-06	5520	5510	5450	40	40	2.275 ± 0.007	5450
al04	144	348	0.1	2.256 ± 0.007	0.1346 ± 0.0009	1.12e-04 ± 3e-06	6670	6670	6600	50	50	2.280 ± 0.007	6600
ag05	186	450	0.1	2.191 ± 0.007	0.1446 ± 0.0008	7.6e-05 ± 2e-06	7400	7400	7330	40	40	2.216 ± 0.007	7330
al06	211	611	0.1	2.269 ± 0.007	0.1568 ± 0.0008	7.0e-05 ± 2e-06	7760	7760	7690	40	40	2.297 ± 0.007	7700
aw36	216	583	0.2	2.208 ± 0.007	0.1537 ± 0.0008	9.0e-05 ± 2e-06	7820	7820	7750	40	50	2.234 ± 0.007	7750
cd1-kt3	220	258	2.0	2.124 ± 0.008	0.1547 ± 0.0008	2.5e-03 ± 1.2e-05	8190	8060	7990	130	130	2.150 ± 0.008	7990
aw22	223	334	0.0	2.071 ± 0.007	0.1528 ± 0.0011	4.7e-05 ± 3e-06	8300	8300	8230	60	60	2.098 ± 0.007	8220
aw32	226	490	0.5	2.062 ± 0.007	0.1526 ± 0.0008	3.02e-04 ± 2e-06	8330	8320	8250	50	50	2.087 ± 0.007	8240
al07	243	599	0.1	2.094 ± 0.007	0.1580 ± 0.0008	8.0e-05 ± 2e-06	8500	8500	8430	50	40	2.120 ± 0.007	8440
ag04	262	576	0.1	2.006 ± 0.007	0.1568 ± 0.0008	5.3e-05 ± 2e-06	8820	8810	8750	50	50	2.032 ± 0.007	8750
an15	285	717	0.1	2.002 ± 0.007	0.1659 ± 0.0008	3.8e-05 ± 3e-06	9370	9370	9300	70	60	2.029 ± 0.007	9300
al08	---	669	0.6	2.06 ± 0.007	0.448 ± 0.002	2.9e-05 ± 2e-06	26172	26200	26100	120	120	2.141 ± 0.007	---
al09	---	231	0.1	1.941 ± 0.007	1.015 ± 0.004	1.40e-04 ± 4e-06	75309	75300	75200	400	400	2.163 ± 0.008	---
ag02	---	271	0.3	1.828 ± 0.006	1.273 ± 0.004	3.24e-04 ± 3e-06	115250	115200	115100	700	900	2.147 ± 0.007	---
ag01	---	304	0.2	1.744 ± 0.005	1.271 ± 0.004	2.38e-04 ± 2e-06	125062	125000	124900	800	900	2.058 ± 0.007	---

Table 1. Table 1. Measured U/Th isotope activity ratios and calculated ages.

Table 1 footnote

Sample ID labels begin with a two-letter pair (aa, ab, etc.) that define the sample batch followed by a two-digit number specifying the sample number in the particular batch. Measured isotope ratios are given in activity format, where i.e. (234/238) = (N234*λ234)/(N238*λ238). Uncorrected ages were calculated ignoring any initial ^{230}Th or ^{234}U from detrital contaminants. Ages were calculated using half-lives found in Cheng et al. (2013). Corrected ages were calculated using an initial $^{230}Th/^{232}Th$ atomic ratio of 0.5-10.8 ppm (uniform distribution). Age before 1950 C.E. is given. 95% confidence intervals for the ages are calculated using an internally developed Monte Carlo simulation (available upon request) with N=1e4. Initial (234/238) was calculated using the corrected age. The Oxcal modeled mean age before 1950 C.E. is provided in the last column.

Petrography was done using 8 standard thin-sections, and samples for stable isotope analysis were drilled at 1 mm spacing through the axial part of the stalagmite (287 samples). Isotopic analyses (University of East Anglia Stable Isotope Laboratory) were made on 75±5 µg samples, run alongside 75±5 µg internal standards of UEACMST (University of East Anglia Carrara Marble Standard; $\delta^{18}O$ -2.05 ‰$_{VPDB}$; $\delta^{13}C$ 1.99 ‰$_{VPDB}$), reacted with 105% (ρ = 1.92 gml-3) phosphoric acid (H_3PO_4) at 90°C in an on-line common acid bath. The evolved CO_2 was purified and analysed for $\delta^{18}O$ and $\delta^{13}C$ using a Europa SIRA II dual inlet isotope ratio mass spectrometer. The data are calibrated to international reference scales (VPDB and VSMOW) using IAEA Certified Reference Material NBS-19 ($\delta^{18}O$ -2.20 ‰$_{VPDB}$; $\delta^{13}C$ 1.95 ‰$_{VPDB}$). Repeat analysis of both international and internal reference materials gave 1σ errors of less than ±0.1‰ for both $\delta^{18}O$ and $\delta^{13}C$. Isotope data discussed in the text are relative to VPDB unless indicated otherwise. Single point data outliers were verified with duplicate samples.

Samples for trace element analysis were drilled at 10 mm spacing through the axial part of the stalagmite (30 samples) principally to ascertain their relationship (or otherwise) with $\delta^{13}C$ (see McDermott 2004). 2.5 mg of calcite was dissolved in 5 ml of 10% acetic acid, and then diluted to 50 ml with MilliQ water. Samples, along with international reference standard 'CRM00028 calcite' were analysed on a Varian ICPOES. Raw data were normalised to 100% calcite and are presented in both ppm and molar concentrations. Precision was ± 0.82 µg l^{-1} Mg, ± 0.10 µg l^{-1} Sr, ± 0.20 µg l^{-1} Ba and ± 17 µg l^{-1} P; limit of detection was 49 mg l^{-1} Mg, 6 mg l^{-1} Sr, 12 mg l^{-1} Ba and 1024 mg l^{-1} P.

4. Results

Stalagmite KT-3 is composed of dense, vug-free crystalline calcite. A hiatus at 304 mm dft (distance from top) marks the boundary between pre-Holocene brown, laminated, crystalline calcite, and translucent yellow calcite of Holocene age, the latter devoid of obvious macro-fabrics. Uranium concentration in the stalagmite is ~700 ppb at the beginning of the Holocene and falls to ~200-300 ppb near its active top. KT-3 is extremely clean of detrital contamination, with ^{232}Th concentrations around only 0.1-0.2 ppb. Thus, the U/Th ages are very precise, Holocene 2-sigma age errors between 40-50 years. Vertical extension rate in KT-3 is fastest in the early Holocene, ~40-60 μm/yr until ~6.50 ka, slowing in the mid-Holocene (~6.50-3.50 ka) to ~20-30 μm/yr, and to (10-15 μm/yr) from ~3.0-1.0 ka. Over the past millennium, vertical growth returned to 30-40 μm/yr.

Stalagmite diameter increased significantly following Holocene re-initiation of growth with a maximum width of 90 mm; after this, width decreases steadily upward reaching a final width of 33 mm at the top.

4.1. Petrography

The Holocene part of KT-3 is mostly columnar calcite devoid of internal micro-structure and with few fluid inclusions. The hiatus at 304 mm dft is marked in thin section by a 200 μm thick zone of near-equant calcite microspar crystals ~50 μm wide (Fig. 5a). In places, these small crystals define the upper edges of the much larger underlying crystal terminations; they appear to be included within the basal parts of larger crystals above the hiatus. All these crystals have similar angles of extinction suggesting only a slight difference in optical continuity (Fig. 5a; cf. Frisia 2015, fig. 1c)

From the hiatus to 163 mm dft the calcite is mostly columnar (C) fabric (Frisia 2015), with crystals 100 to 600 μm long axis with upward elongation of axial crystal c-axes , often with curved, slightly irregular boundaries and rounded terminations (Fig. 5b). From 163 mm dft to the top of the stalagmite a columnar elongated (Ce) fabric (Frisia 2015) is typical (Fig. 5c). These Ce crystals are >1.3 cm long and between 200 μm to nearly 1 cm wide, with planar intercrystalline boundaries and angular terminations. There is a slight increase in irregularity of some boundaries and some shortening of columnar crystals near the top of the stalagmite. Crystals at the stalagmite ‘tip’ are neither eroded nor corroded. Additional petrographic details are given in the Supplementary Information and Figure S1.

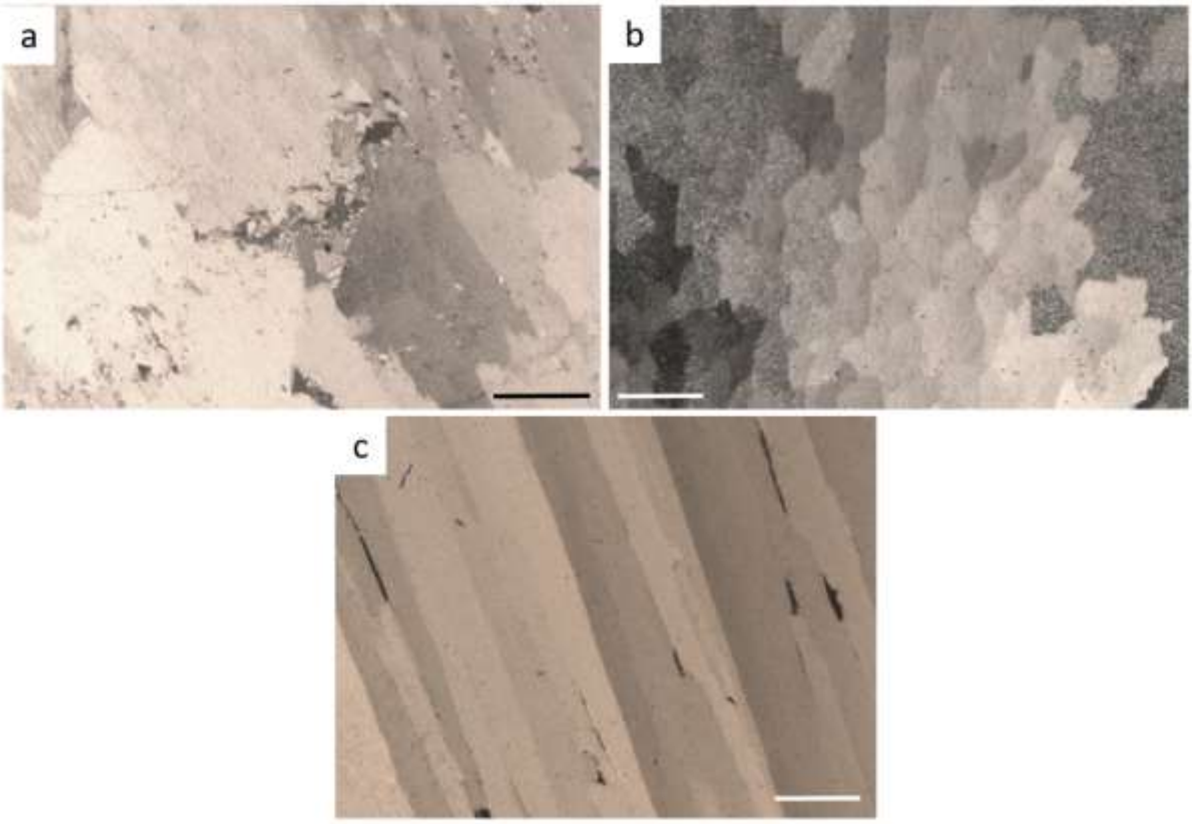

Fig. 5. Thin section photomicrographs (crossed polars) of typical KT-3 fabrics with 500 μm scale bars. a) Equant to angular microspar marking hiatus at 304 mm dft; note slight differences in extinction angles between microspar and surrounding C calcites; b) short columnar crystals just above hiatus at 304 mm dft; c) Elongate C calcite above 163 mm dft with intercrystalline porosity (dark areas).

4.2. Geochemistry

Between 9.5 and 7.0 ka $\delta^{18}O$ values range between -10.0 and -9.5‰ (Fig. 6); after 7.0 ka values steadily increase until around 3.0 ka, when they stabilise at ~-8.0‰ and remain so until the present day. This overall trend is punctuated by two positive single point outliers of ~1.0‰ at 9.4 and 7.5 ka, and two negative spikes ~0.5‰ at 8.5 and 8.1 ka.

At 9.5 ka, initial $\delta^{13}C$ values are ~-2.8‰, steadily declining to ~-4.0‰ at 4.4 ka (Fig. 7), albeit with centennial-scale periods of lower and higher values (~1.0‰ scale changes). The largest positive excursion (~1.8‰) in this period begins ~8250 years BP, peaking at

7740 years BP and finishing ~7700 years BP. Values increase markedly between 4.4 and 3.0 ka (to ~-2.5‰), before recovering to ~-5.0‰ at the present day.

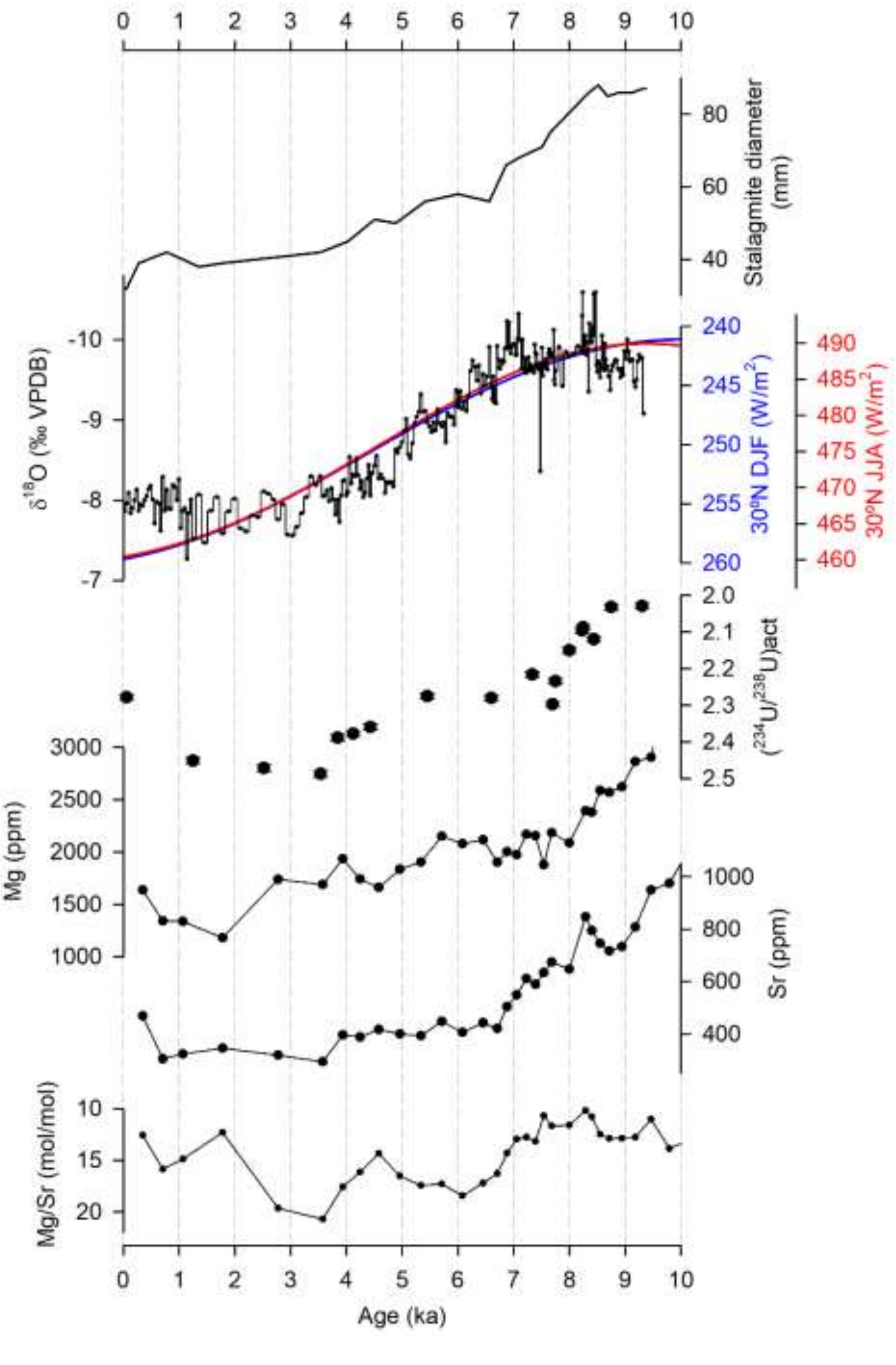

Fig. 6. KT-3 Holocene data series: stalagmite diameter, $\delta^{18}O$, $U^{234/238}$ and trace elements compared to 30°N summer (red) and winter (blue) insolation. Note Mg/Sr data are plotted on a reversed scale for easier comparison with $\delta^{18}O$ variation.

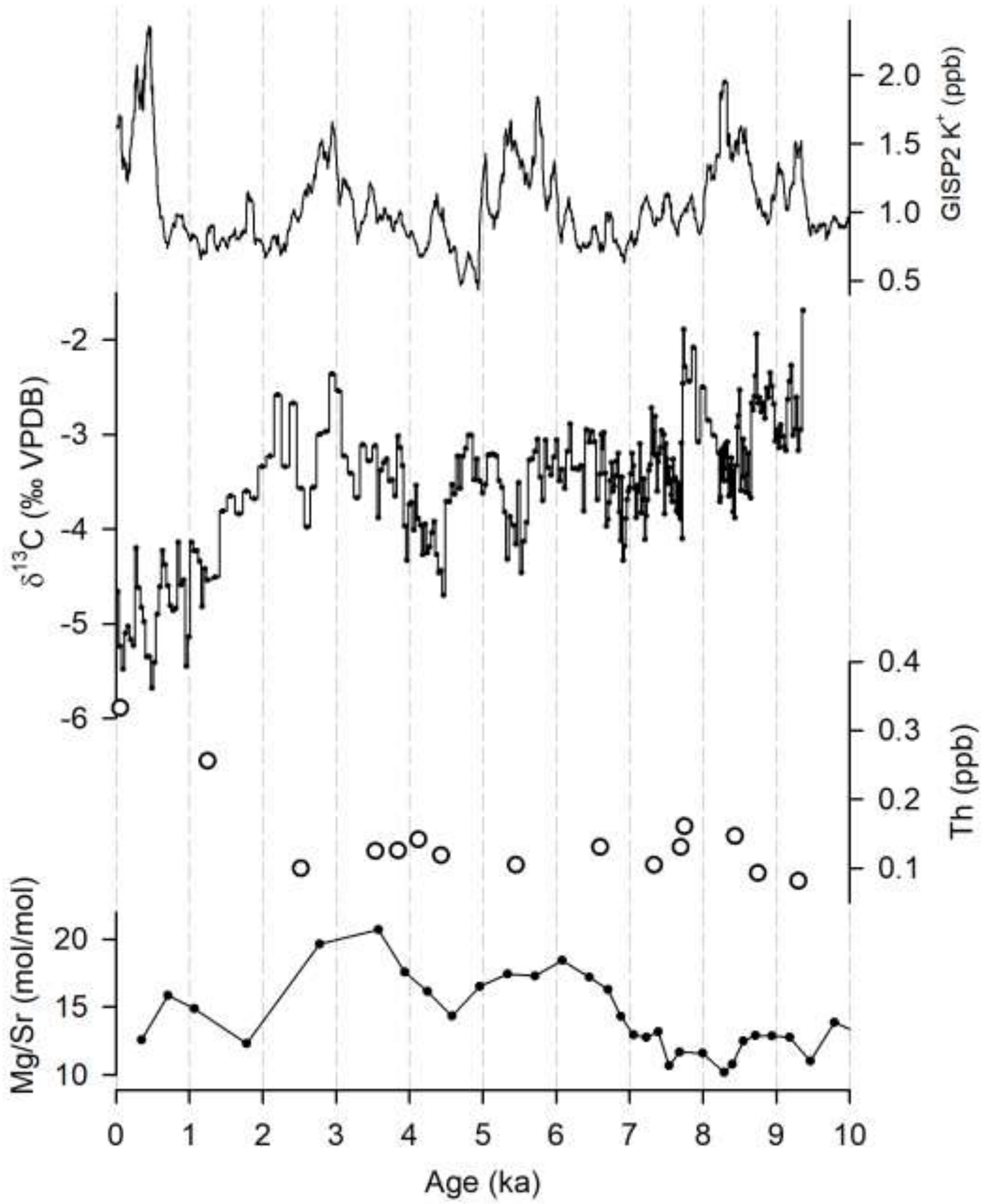

Fig. 7. KT-3 Holocene data series: $\delta^{13}C$, Th content and Mg/Sr compared to the GISP2 non-sea-salt K^+ record (Mayewski et al., 1997).

Mg and Sr contents are strongly correlated (r^2 0.86; Fig. S2) and broadly decrease with time (Fig. 6); both elements decrease by >50% of their initial values (4000 ppm Mg; 1000 ppm Sr) in the early Holocene between 9.5 and 7.0 ka, before more gradual declines (2000 to 1200 ppm for Mg; 600-300 ppm for Sr) to the present day values. Ba contents between 140 and 55 ppm, while variable, have a profile similar to Sr (r^2 0.44; Fig. S3). Some of the ‘peakiness’ in the Ba record corresponds with peaks in P, (Fig. S3) particularly between 8.5 and 7.0 ka.

Decreasing Mg and Sr content correspond broadly with increasing $\delta^{18}O$ (Fig. 6; weak negative correlation with R^2 of 0.26 and 0.40 respectively) but show no clear relationship with $\delta^{13}C$. Ba shows a similar overall relationship with $\delta^{18}O$ as Mg and Sr but at much lower concentrations. Molar Mg/Sr is not strongly related to $\delta^{18}O$ variation (Fig. 6), but neither is the ratio constant, suggesting a mixed control on one or both elements (Tremaine and Froelich 2013). Mg/Sr increases steadily from ~13 at 8.0 ka to ~18 at 6.0 ka; values then decrease to ~15 until 4.5 ka, then increase again to ~20 between 3.6-2.8 ka when $\delta^{13}C$ is also enriched (Fig. 7). Mg/Sr then decline again to ~14 after 2.5 ka (Fig. 6).

5. Interpretation

5.1. Stable isotopes background

Katalekhor Cave lies in an area for which very little precipitation or groundwater isotopic data is available and Iran’s size, topography and diversity of moisture sources preclude the development of a single meteoric water line (MWL) with wide application. Three regional MWLs have been recently calculated for Northern Iran, Western Zagros and Southern Zagros, zones defined by different combinations of dominant air masses (Heydarizad et al., 2019): Katalekhor Cave is located between the core areas of the Northern and Western zones. Interpolated monthly precipitation isotopic values (OIPC v3.1 www.waterisotopes.org; Bowen and Wilkinson 2002; Bowen and Revenaugh 2003; Table S1) show strong seasonal differences (Fig. 8) which reflect rainfall amounts, atmospheric temperature, moisture source and air mass trajectories. The OIPC MWL has a lower slope than both the Global and Mediterranean MWLs (Fig. 9) and represents a best fit regression line through interpolated isotopic data derived from precipitation events associated with air masses of very diverse origins and flow paths (see above). It is therefore difficult to interpret the line in terms of vapour source or atmospheric processes.

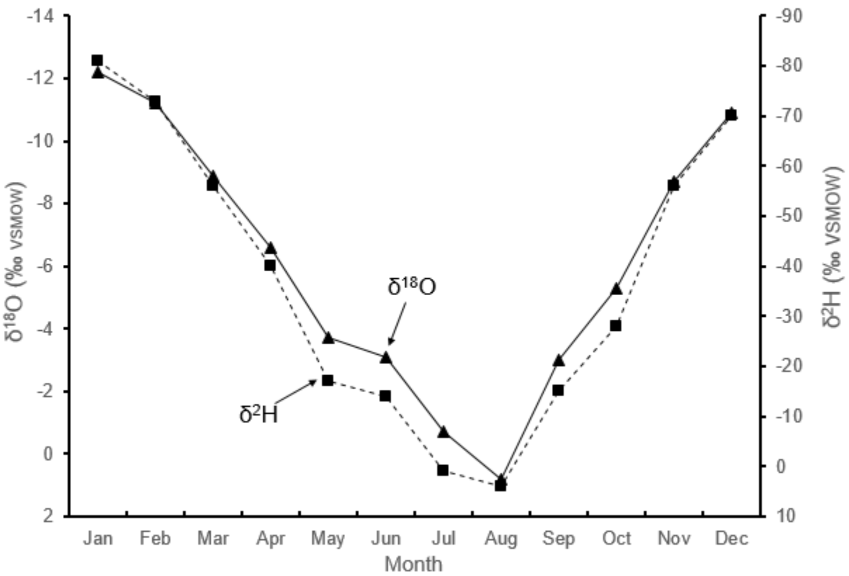

Fig. 8. Seasonal variation in oxygen (solid line) and hydrogen (dashed line) isotopes in Katalekhor precipitation based on interpolated OIPC data (Table S1).

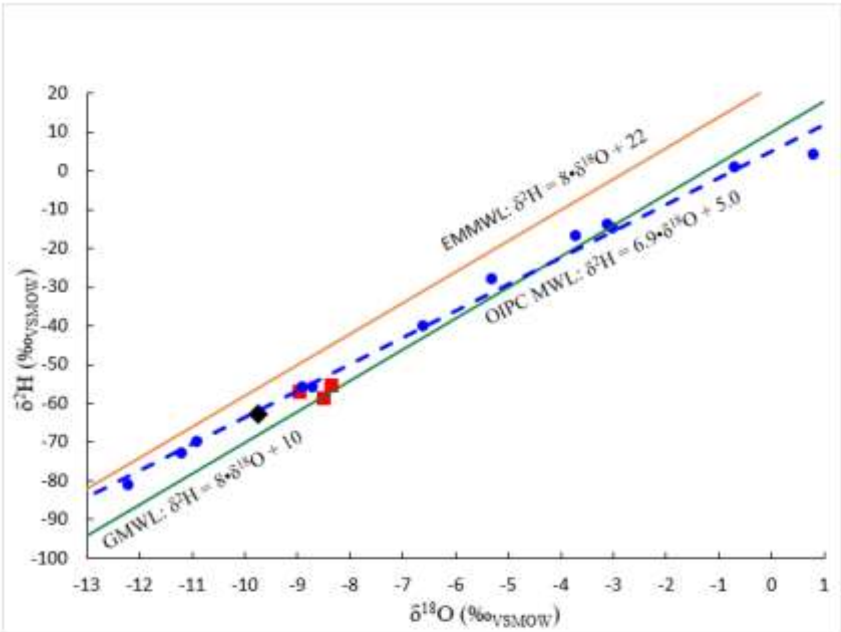

Fig. 9. Local Meteoric Water Line for Katalekhor Cave site (blue dashed line) from interpolated OIPC monthly isotopic values for precipitation at the Katalekhor Cave site (blue dots). Black diamond shows mean OIPC November-April isotopic composition of precipitation. Red squares are Katalekhor Cave water samples collected November 2006 (Table S2). Also plotted for context are the Global Meteoric Water Line (green; Craig, 1961) and the Eastern Mediterranean Meteoric Water Line (orange; Gat and Carmi, 1970).

Three drip and pool waters sampled at the time of stalagmite collection (November 2006) have $\delta^{18}O$ between -8.4 and -9.0‰$_{VSMOW}$ (Table S2) and plot on or just above the GMWL but below the MMWL (Fig. 9). These compositions are within error of the OIPC mean November interpolation (-8.7‰$_{VSMOW}$) and slightly less negative than the OIPC inferred non-weighted mean winter/spring (NDJFMA) recharge value of -9.75‰$_{VSMOW}$ (Table S2). The two drip water samples are slightly enriched relative to the pool sample, which may reflect mixing of autumn recharge with residual water in the epikarst.

November 2006 drip water supplying KT-3 had $\delta^{2}H$ -55.4‰$_{VSMOW}$ and $\delta^{18}O$ -8.4‰$_{VSMOW}$ (Table S2 and Fig. 9). Calcite from the growth tip had a $\delta^{18}O$ of -7.9‰$_{VPDB}$. These data allow calculation of the extent of oxygen isotopic equilibrium during active KT-3 calcite precipitation. To do this we used the best-fit "cave calcite" line through a plot of the available global speleothem-water $\delta^{18}O$ data (Tremaine et al., 2011) described by the equation:

$$1000\ln\alpha = 16.1\ (10^{3}T^{-1})\ -24.6 \qquad (1)$$

This relationship implies that water-calcite equilibrium fractionation factors are higher in natural cave systems than in laboratory experiments (see also Daëron et al., 2019). The calculated temperature using the Tremaine et al. (2011) equation is 16.7 ºC, close to the measured chamber air temperature of 15.5 ºC - 16.6 ºC during sampling (Section 2). The data suggest that KT-3 calcite is forming in near-equilibrium with its modern drip waters and we assume these conditions largely held during the Holocene. Drip waters with a stronger component of winter precipitation lower calculated temperatures. For example, an equilibrium temperature calculated from the averaged last 500 years of KT-3 calcite growth ($\delta^{18}O$ -8.0 ‰$_{VPDB}$) and modern non-weighted mean winter/spring (NDJFMA) drip water recharge ($\delta^{18}O$ -9.75 ‰$_{VSMOW}$) is 10.3 ºC. This temperature is comparable to a modern mean annual temperature (1986-2005) of 10.6 ºC at nearby Zanjan, Iran (1663 m; Kisi and Shiri 2014).

5.2. KT-3 petrography

Early Holocene extension of KT-3 (9.5-6.5 ka) was faster (~40-60 μm/yr) than all later extension (6.5 ka onward) except the last millennium. The KT-3 extension rate also dropped significantly to ~14 μm/yr for a short period between 8.24-7.81 ka. Marked thinning of the stalagmite diameter began ~8.4 ka and progressive thinning from this time onward indicates reducing drip rate with time. While lack of intra-Holocene growth hiatuses suggests no cessation in drips, the change from C to Ce fabrics at 163 mm dft (~6.7 ka) is coincident with the switch to slower extension rate.

The small crystals above the basal hiatus are interpreted as random growth fabrics associated with nucleation (Frisia 2015), followed by overgrowth of C crystals. The irregular crystal boundaries seen to 163 mm dft indicate interference of growth between neighbouring crystallites (Kendall and Broughton 1978). Such changes in stacking are due to crystallite defects caused by the presence of growth inhibitors such as organic materials or by rapid extension rate (Frisia et al., 2000; Frisia and Borsato 2010). These fabrics may therefore indicate a relatively fast drip rate during first ~4000 years of Holocene growth, which is consistent with rapid stalagmite extension (indicated by the age model) and the wider stalagmite diameter. It is also possible that the higher Ba contents registered until 7.2 ka indicate a link to delivery of organic derived colloidal particles (Borsato et al., 2007), potentially indicative of efficient epikarst flushing.

The columnar elongated (Ce) fabrics above 163 mm dft (after ~6.7 ka) have straight, well-defined boundaries created by more regular stacking of crystallites (Frisia et al., 2000). Larger crystals with stable boundaries grow under constant drips (Frisia 2015), but in KT-3 the association of Ce fabrics with a diminishing stalagmite diameter suggest a gradually reducing drip water volume. Relationship between KT-3 Ce fabric and higher drip water Mg/Ca ratios (Frisia et al., 2000; Frisia 2015) is not expected as the Ce calcite Mg content is lower than that of the earlier formed C calcites (see below).

5.3. Geochemistry

In the Mediterranean, orbital precession has a strong influence on climate with high summer and low winter insolation favouring hotter and drier summers and cooler wetter winters (Fletcher and Sánchez Goñi 2008). In Iran, reduction in winter rain may also be influenced by a strong winter Siberian high pressure system that develops when summer solar insolation is at a minimum and winter insolation at maximum (Miller et al., 2005). The progressive increase in Holocene $\delta^{18}O$ after 7.0 ka in KT-3 tracks the decrease in summer insolation (Fig. 6). This increase in $\delta^{18}O$ is driven by hypothesized gradual reduction in winter precipitation amount as seen clearly in a stalagmite from Uzbekistan (Tonnel'naya Cave; Cheng et al., 2016), and suggested in a NW Iranian stalagmite from Qal'e Kord Cave

(Fig. S4: Mehterian et al., 2017) 125 km from Katalekhor. There was no growth of KT-3 at the summer insolation maximum around 11.5 ka. Even after Holocene growth initiation at 9.5 ka, KT-3 $\delta^{18}O$ does not immediately increase coincident with summer insolation reduction in the way that Tonnel'naya Cave $\delta^{18}O$ does after 10 ka (Cheng et al., 2016). KT-3 $\delta^{18}O$ values between 9.5 and 8.5 ka (Fig. 6) are thus less negative than expected for an insolation driver (cf. Tonnel'naya Cave; Cheng et al., 2016) in the early Holocene, suggesting that winters were not as wet as they might have been had insolation been the dominant forcing. The indicated delayed regional response to insolation forcing, by around 1000 years, could have resulted from the glacial boundary conditions, particularly enhanced Eurasian snow cover. Snow cover supresses insolation effects due to its higher albedo and in particular by consuming energy during melting and associated hydrological effects (Barnett et al., 1988; Ye and Bao, 2001). Alternatively, reduced early Holocene regional rainfall may have been influenced by postglacial sea-level recovery in the Persian Gulf. Between 10.0 and 8.0 ka the gulf sea surface area was much reduced relative to today (Lambeck 1996), which may have affected cyclogenesis and thus regional rainfall amount.

Increased time interval between drips leads to reduction in stalagmite diameter (Kaufmann 2003) consistent with increasing $\delta^{18}O$ values indicating decreasing precipitation amount (Fig. 6). Rate of diameter reduction from 7.0 ka onward mimics the increase in $\delta^{18}O$ caused by insolation forcing (Fig. 6). Increase in $^{234}U/^{238}U_0$ activity ratios from around 2.0 in the early Holocene to ~2.4 in the late Holocene (Table 1; Fig. 6) also follows the $\delta^{18}O$ profile. In arid regions, $^{234}U/^{238}U_0$ may reflect the relative contribution of U from soil versus that from bedrock dissolution, controlled by epikarst residence time and discharge rate (Kaufman et al., 1998; Rowe et al., 2020) which is thus climatically driven.

While KT-3 $\delta^{18}O$ is indicating progressive reduction in winter precipitation amount after 7.0 ka, it is notable that centennial-scale variability is not a feature. For example the distinct ~1‰ negative $\delta^{18}O$ spike ('Assyrian megapluvial') at 2800-2690 years BP in Kuna Bar cave stalagmites of the Tigris floodplain area (Sinha et al., 2019) 260 km SW of Katalekhor, has negligible expression in KT-3. The Tigris area is on the SW margin of the Zagros winter precipitation zone (Evans and Smith 2006) where interannual rainfall variability is between 40-60% (Sinha et al., 2019), thus both flood and drought prone. In contrast Katalekhor is situated in the core area of stable winter recharge where interannual rainfall variability is less marked or absent.

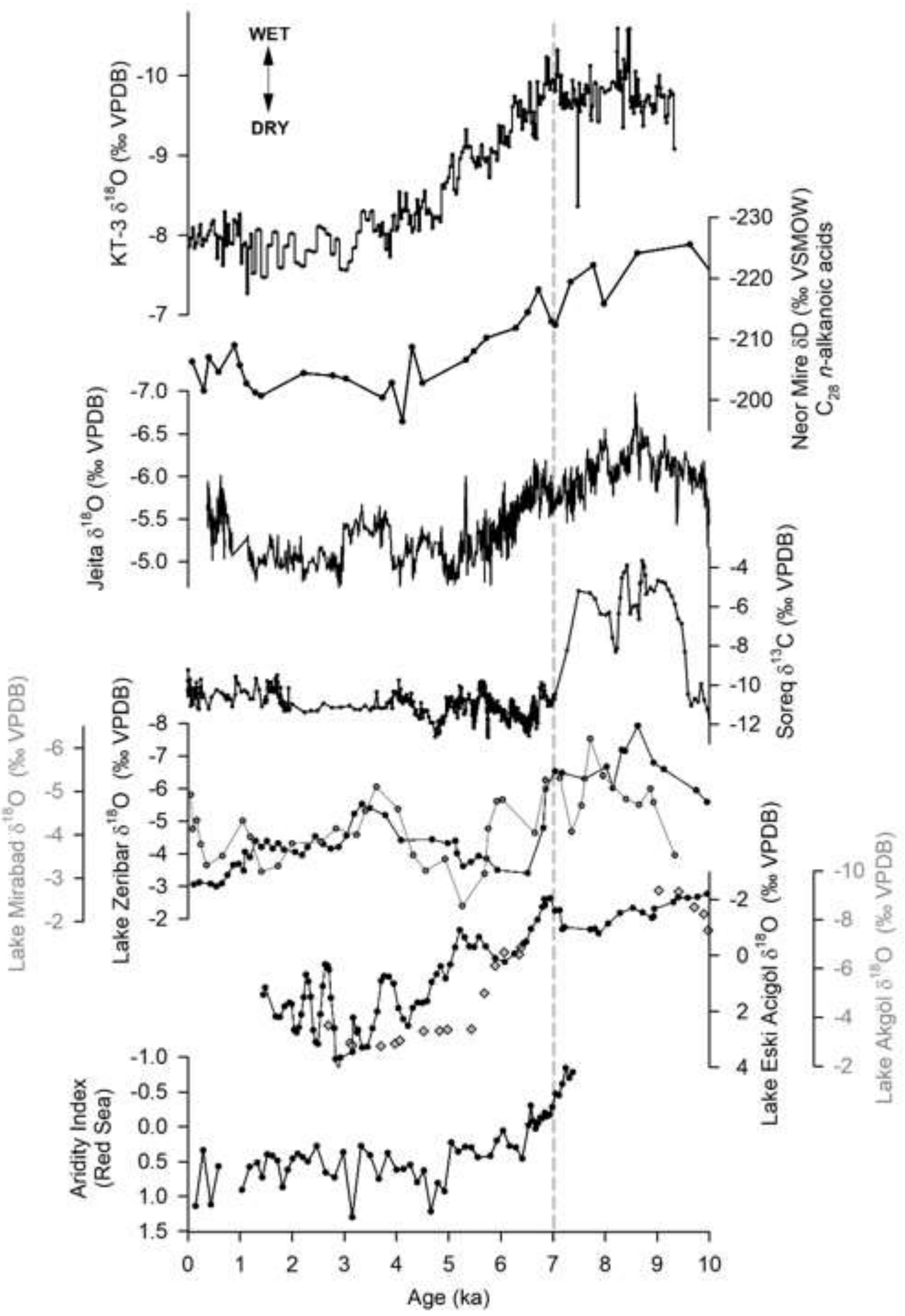

Fig. 10. KT-3 $\delta^{18}O$ record compared with other regional Holocene palaeoclimate records from Neor Mire (Iran; Sharifi et al., 2015), Jeita Cave (Lebanon; Cheng et al., 2015), Soreq Cave (Israel; Bar-Matthews et al., 2003; Grant et al., 2012), Iranian lakes Mirabad and Zeribar (Stevens et al., 2001; 2006), Turkish lakes Eski Acigöl (Roberts et al., 2001) and Akgöl (Leng et al., 1999) and Red Sea aridity index from Arz et al., (2003).

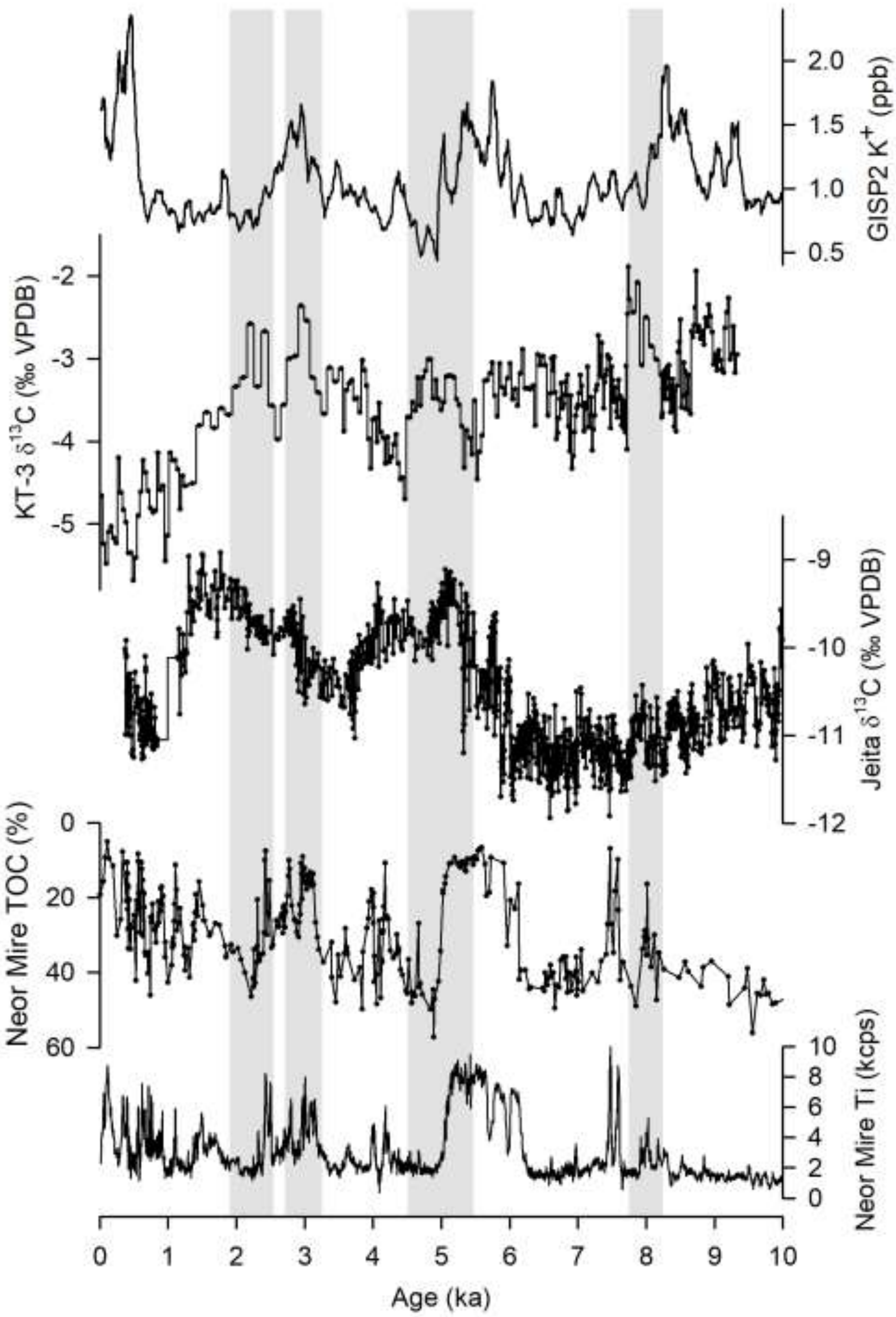

Fig. 11. KT-3 δ^{13}C record compared to aridity signals in the GISP2 non-sea-salt K^{+} record (Mayewski et al., 1997), Jeita Cave δ^{13}C record (Lebanon) and Neor Mire (Iran) TOC and Ti data (Sharifi et al., 2015). Grey bars highlight periods of aridity in KT-3 δ^{13}C.

The $\delta^{13}C$ values broadly decrease between 9.5 and 4.4 ka (Fig. 7), but unlike $\delta^{18}O$ there is centennial scale variability with higher $\delta^{13}C$ (<1.5‰) values between 8.3-7.7 ka, 6.5-5.5 ka, 5.4-4.5 ka and ~4.3-2.0 ka (including distinct peaks ~3.0 and 2.2 ka). After 2.0 ka $\delta^{13}C$ show a marked 1.5‰ decrease to modern values, at about the time that local summer insolation stabilizes near a relative minimum (Fig. 7). Overall KT-3 $\delta^{13}C$ compositions are enriched relative to lower altitude stalagmite records at Soreq (Israel; Fig. 10), Jeita (Lebanon; Fig. 11) and Kuna Ba (Iraq) where more negative $\delta^{13}C$ indicate stronger influence of soil CO_2 (Verheyden et al., 2008; Bar-Matthews and Ayalon 2011: Sinha et al., 2019). We interpret the KT-3 values to reflect a low soil CO_2 contribution (modern soil development at the cave is sparse) where short soil–water residence time prevents complete isotopic equilibration between soil CO_2 and infiltrating water. This allows a stronger ingress of atmospheric CO_2 (cf. Genty et al., 2003) with heavier isotopic composition (Holocene atmospheric CO_2 $\delta^{13}C$ ~ -6.5‰; Elsig et al., 2009), possibly also modulated by variable limestone bedrock weathering contributions (McDermott 2004). The ~ 1.5‰ centennial scale variability in the KT-3 $\delta^{13}C$ record is probably thus controlled mainly by either small changes in soil development (more negative values reflecting some soil development), or periodic dryness or ground freezing/snow covered conditions that impart an 'aridity' signal. Viewed on a millennial scale, net soil development between 9.5 and 4.0 ka (Fig. 7) was marginal, but deteriorating during the centennial-scale dry periods. The first of these was between 8.3-7.7 ka (Figs 11 & 12): a 550 year period that overlaps both the ~160 year-long, 8.2 ka cold/dry event (Alley et al., 1997; Clarke et al. 2004; Alley and Ágústsdóttir 2005) and the latter part of a Rapid Climate Change (RCC) event based on non-seasalt potassium (K^+) in Greenland ice cores (Mayewski et al., 2004). The RCC between 9.0-8.0 ka gave rise to an intensified Siberian High Pressure that affected Mediterranean regional climate (Rohling et al., 2019), including reduced SST until ~7.8 ka in some eastern Mediterranean records (Rohling et al. 2002; Marino et al, 2009). The broad reversal in KT-3 $\delta^{13}C$ trend, beginning around 4.3 ka and ending soon after 2.0 ka (Fig. 11) similarly marks sustained aridity. This period includes peaks in $\delta^{13}C$ ~3.4 and 2.2 ka that also correspond with a RCC event between 3.5-2.5 ka (Mayewski et al., 2004). It also encompasses the 2.65 to 2.50 ka 'Assyrian megadrought' event evident in both $\delta^{13}C$ and $\delta^{18}O$ records from Kuna Bar cave (Sinha et al., 2019). Cessation of cold and dry conditions in KT-3 after 2.2 ka were followed by amelioration toward present day conditions.

The similarity of the $^{234}U/^{238}U_0$ activity profile with those of Mg, Sr (Fig. 6) and Ba suggest that the source of these trace elements in drip water is controlled principally by limestone bedrock dissolution (Fairchild et al., 2010). The initially high Sr and Mg may indicate flushing of epikarst water with a legacy of bedrock regolith (and possibly soil) dissolution that had built up in the arid conditions preceding the Holocene. The $\delta^{13}C$ values at this time are, however, at their least negative, suggesting low soil CO_2 contribution.

Initial flushing reduced drip water Sr and Mg within a few centuries and thereafter broad anti-correlation between $\delta^{18}O$ and both Mg and Sr (Fig. 6) is not explained by either an epikarst residence time or prior calcite precipitation (PCP) control, where an opposite 'aridity' relationship with Mg and Sr would be expected (Fairchild et al., 2000). Lack of any clear relationship between Mg and $\delta^{13}C$ thus casts doubt on strong residence time or PCP influence on drip water compositions. The strong covariation between Sr and Ba (but not Mg), in a high-resolution record between 5.0-3.8 ka (Fig. S2), further supports their supply from limestone bedrock (Fairchild et al., 2010), while Mg probably has more complex sources (Rutlidge et al. 2014). Variability in molar Mg/Sr and comparison of the Mg and Sr profiles (Fig. 7.15) demonstrates that a component of Mg supply is from a non-bedrock source (Tremaine and Froelich 2013; Rutlidge et al., 2014). Increased molar Mg/Sr between 6.6-5.0 ka and again between 4.0-2.5 ka suggests an increase in non-limestone-derived Mg. These timings concur with RCC's seen in the non-seasalt potassium (K^+) in Greenland ice cores (Fig. 7) suggesting that aeolian dust may be the source (cf. Carolin et al. 2019). Elevated molar Mg/Sr between 4.0-2.5 ka also corresponds with higher with higher KT-3 $\delta^{13}C$ (Fig. 7), both indicating aridity.

P in speleothems is typically related to organic matter content (Borsato et al., 2007); peaks in KT-3 P are thus probably controlled by episodic leaching of organic matter from soils. Covariation of peaks in P and Ba, particularly between 8.5 and 7.0 ka (Fig. S3), shows that background Ba is augmented episodically by a soil organo-colloidal source (Borsato et al., 2007; McDonald et al., 2007; Rutlidge et al., 2014).

The change to more negative $\delta^{13}C$ after 2.0 ka, coincident with lowest summer and least cold winter temperatures based on the insolation records, could indicate decreasing effective evaporation (without change in precipitation amount) that reduced epikarst residence time (lower bedrock carbon contribution). Improved soil-moisture availability would also have allowed better vegetation development. The highest ^{232}Th contents of the record at this time suggest a strong wind-borne dust supply, as do the Mg/Sr ratios (Fig. 7), but local aridity is not indicated in the $\delta^{13}C$ values.

6. KT-3 Holocene palaeoclimate: regional comparisons

In KT-3 the $\delta^{18}O$ values indicate a wet early Holocene (9.5 to 7.0 ka), hypothesized as wet winters. This is consistent with the regional-scale scenario (Burstyn et al., 2019), including the notion of a northward displacement of the westerly jet axis at times of high solar insolation over West Asia (Cheng et al., 2016; Mehterian et al. 2017), corresponding with a strong Asian summer monsoon. The KT-3 $\delta^{18}O$ record also suggests that snow cover damped the regional early Holocene response to insolation forcing (Section 5.3), consistent with a similar delayed early Holocene response of the Indian Summer Monsoon to insolation recorded in stalagmites from Oman (Fleitmann et al., 2007).

Initiation of KT-3 growth was coincident with onset of sapropel 1 (S1) ~9.5 ka in the Levantine Basin (Almogi-Labin et al., 2009). Lake and speleothem records in Iran (Mirabad and Neor mire; Stevens et al., 2006; Sharifi et al., 2015), Turkey (Van and Karaca; Wick et al., 2003; Rowe et al., 2012), Egypt (Sun et al., 2019) and the Levantine Basin itself (Emeis et al., 2000), all indicate wet conditions at this time (Fig. 10). After 7.0 ka, a strong insolation control is evident in reduction in stalagmite diameter, increase in $\delta^{18}O$ values, and reduction in $^{234}U/^{238}U$ values all indicating progressive precipitation amount reduction leading to a much drier mid-late Holocene conditions. This trend is clear in other Iranian (Walker & Fattahi 2011; Jones et al., 2008; Sharifi et al., 2015) and wider Eastern Mediterranean/Middle Eastern palaeoclimate records (e.g. Bar-Matthews et al., 1997; Frumkin et al., 1999; Arz et al., 2003; Eastwood et al., 2007; Cheng et al., 2015; Sun et al., 2019).

The KT-3 $\delta^{13}C$ values mostly become more negative between 9.5 and 7.0 ka (Fig. 7) which suggests modest increase in soil CO_2 contribution, in agreement with the most negative Holocene $\delta^{13}C$ values between 10.0 and 7.4 ka in the Soreq Cave record (Bar-Matthews et al., 2003). The transition to drier conditions in KT-3 beginning around ~7.0 ka, (less negative $\delta^{18}O$, reduced stalagmite diameter), followed by reduction in extension rate and the petrographic fabric change ~6.7 ka, correspond with the cessation of Holocene climate optimum indications in Levantine records (Robinson et al., 2006). Specifically (see Fig. 10), a 7.4 ka return to aridity ($\delta^{13}C$, Soreq Cave; Bar-Matthews et al., 2003), increasing $\delta^{18}O$

(aridity) after 6.0 ka in Jeita Cave (Cheng et al., 2015) and cessation of reduced salinity in the Northern Red Sea at 7.2 ka (Arz et al., 2003).

The 550 year enrichment in KT-3 $\delta^{13}C$ between 8.3-7.7 ka (Fig. 12) is a combined record of aridity resulting from the 8.2 ka event, superimposed on an RCC event. The start of this anomaly is coincident with North Atlantic sea-surface temperature reduction at ~8.3 ka (Ellison et al., 2006) caused by meltwater release of glacial lakes Agassiz and Ojibway (Barber et al. 1999; Clarke et al. 2004; Alley and Ágústsdóttir 2005). The KT-3 anomaly is, however, too long to be simply a response to the 8.2 ka event, and is superimposed on a broader RCC climatic anomaly. This event is now well documented in SST records from the eastern Mediterranean and Aegean (Rohling et al. 2002; Rohling and Pälike 2005; Marino et al., 2009) and from isotopic signals in Greek and Alpine stalagmites (Affolter et al., 2019; Peckover et al., 2019). The RCC cooling is attributed to weakening of the Atlantic meridional ocean circulation and reduction in northward heat transport caused by increased flux of meltwater from the Laurentide Ice Sheet into the North Atlantic (Rohling and Pälike 2005). The influence of the melting Laurentide Ice Sheet ended ~7.8 ka, after which more stable continental Europe temperatures re-established (Affolter et al., 2019).

In KT-3 the combined event between 8.3-7.7 ka is only seen in $\delta^{13}C$, combined with a slow-down in stalagmite extension rate, both of which imply aridity. Enhanced input of aeolian dust ~8.0 ka in Iranian Neor peat mire (Sharifi et al., 2015; Fig. 11) supports this interpretation. Despite the near-global climatic effects of the 8.2 ka event (Cheng et al., 2009), its presence in Mediterranean-Fertile Crescent stalagmite isotope records is not consistent (e.g. Frumkin et al., 1994; Bar Matthews et al. 1999; Zanchetta et al., 2007; Verheyden et al. 2008; Cheng et al., 2015; Peckover et al., 2019), rather its record is regionally heterogeneous (Burstyn et al., 2019). Middle Eastern pollen records have not typically captured climate change indications at this time, neither have signs of human disturbance been recognised in archaeological records (van der Horn et al., 2015).

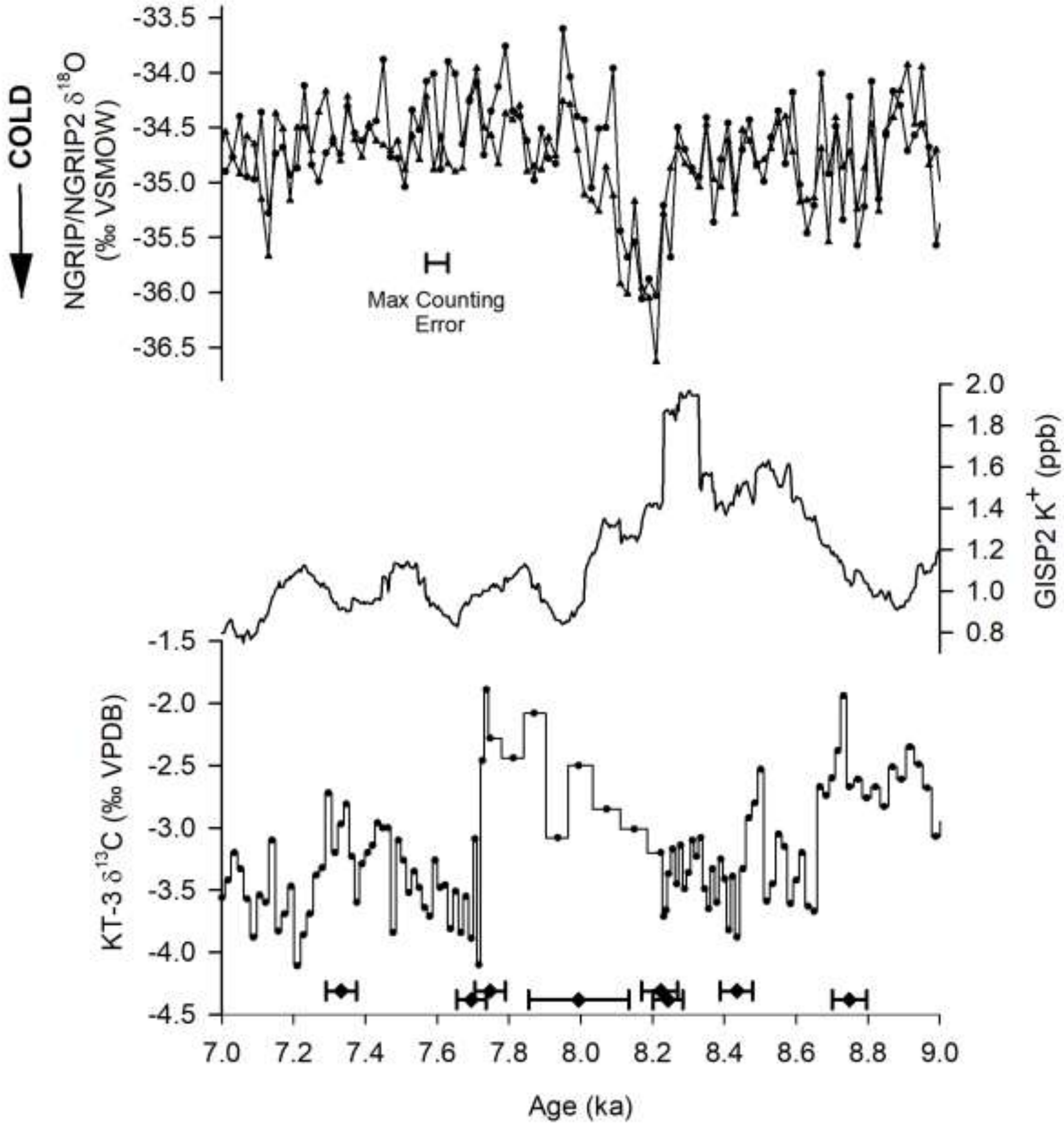

Fig. 12. Detail of KT-3 $\delta^{13}C$ record between 9.0 and 7.0 ka compared to Greenland ice-core $\delta^{18}O$ 8.2 ka anomaly (0-7.9ka age model from Vinther et al., 2006; 7.9-14.7ka age model: Rasmussen et al., 2006; GRIP data: Johnsen et al., 1997; NGRIP data: Dahl-Jensen et al., 2002) and the GISP2 non-sea-salt K^+ record (Mayewski et al., 1997). Position of KT-3 U/Th dates with error bars (Table 1) indicated above the age axis.

Regional palaeoclimate records after 6.0 ka largely corroborate the reduction in rainfall and developing aridity seen in KT-3 $\delta^{18}O$. However, centennial-scale changes in the KT-3 $\delta^{13}C$ indicate switches from relatively cold and dry to slightly warmer and wetter conditions (Fig. 11). Increase in KT-3 $\delta^{13}C$ between 5.4 and 4.5 ka matches that seen in the Levant, where millennial-scale dryness is evident between 5.3-4.2 ka (centred ~5.1 ka; Fig. 11) in Jeita Cave (Cheng et al. 2015). The broad increase in KT-3 $\delta^{13}C$ beginning around 4.3 ka and ending around 2.0 ka, suggests decreasing rainfall amount (decrease in soil CO_2 contribution), supported by continued reduction in growth diameter to 2.2 ka. These generally cold/dry conditions overlap the timing of 'Assyrian megadrought' in both $\delta^{13}C$ and $\delta^{18}O$ records in Kuna Bar cave (Sinha et al., 2019). Distinct peaks in KT-3 $\delta^{13}C$ ~3.0 and 2.2 ka correlate with lithogenic dust proxies in the Iranian Neor peat mire (Sharifi et al., 2015) that correspond with an RCC event of intensified Siberian High Pressure between 3.5-2.5 ka (Mayewski et al., 2004; Fig. 11). This event also has expression in the detrended Jeita Cave $\delta^{18}O$ (Rohling, et al., 2019), and in Syrian alluvial pollen records (Kaniewski et al., 2019). Millennial-scale precipitation decrease ~2.0 ka in Turkey (Dermody et al., 2012) is within dating error of the 2.2 ka KT-3 $\delta^{13}C$ peak and close to the least negative $\delta^{13}C$ at 2.4 ka in Kuna Bar cave (Sinha et al., 2019).

There is no KT-3 trace element record of increased dust flux beginning abruptly at 4.51 and 4.26 ka seen in another Iranian speleothem (Carolin et al., 2019). The very low ^{232}Th (Table 1) in KT-3 indicates largely detritus free-calcite before 2.5 ka. The over-riding impression is that only $\delta^{13}C$ registers centennial or longer period changes such as the 3.5-2.5 ka RCC event and not the abrupt aridity indicators seen in some records (Bar-Matthews and Ayalon, 2011; Carolin et al., 2019; Schmidt et al., 2011), that have been linked directly with North Mesopotamian settlement abandonment or human settlement hiatus in the Iranian Plateau. This said, the increase in KT-3 $\delta^{13}C$ beginning around 4.4 ka and ending around 2.0 ka has a timing that overlaps the 'Crisis Years Cooling Event' that impacted eastern Mediterranean populations through stressors on food and agricultural productivity (Kaniewski et al., 2019; Sinha et al., 2019). Indeed, as noted in the Neor peat mire dust record (Sharifi et al., 2015) aridity at this time overlaps empire collapse (UrIII, Elam and Medes empires) and demise of the Archaemenids.

6.1. Comparisons with lake records from Zeribar and Mirabad

Understanding of regional Holocene palaeoclimate in Iran has until recently been heavily influenced by geochemical, palynological and plant macrofossil data from Iranian Lakes Zeribar and Mirabad (Stevens et al., 2001; 2006) situated 180 km W and 300 km SSW of Katalekhor Cave (Fig. 1). These lake proxies were thought to record changes in seasonality of rainfall (Stevens et al., 2001, 2006); however, this scenario relies heavily on a correct interpretation of the terrestrial pollen data. Other regional palaeoclimate indicators do not concur with this scenario (Roberts et al., 2008; Rowe et al., 2012; Sharifi et al., 2015), in particular the notion of a relatively dry early Holocene (Stevens et al., 2001) and wettest conditions in the Mid Holocene (Stevens et al., 2001, 2006; Griffiths et al., 2001). Neither of these climatic signatures register in KT-3 where a relatively wet early Holocene is followed by increasing aridity in the Mid Holocene.

The Zeribar carbonate isotope records, decoupled from the pollen data, could result from simple covariation in a closed lake basin (Stevens et al., 2001). If so the $\delta^{18}O$ record (and the Mirabad $\delta^{18}O$ record; Stevens et al., 2001) can be interpreted broadly as an insolation-driven record in the early Holocene, starting wet, but with recharge decreasing until ~7.0 ka, followed by developing aridity that increases both $\delta^{18}O$ and $\delta^{13}C$ (Fig. 10). Plant macrofossils from Zeribar are consistent with low salinity freshwater conditions between 10.0-6.9 ka (Wasylikowa, et al., 2006). The early Holocene Sr/Ca in ostracode shells from Mirabad, interpreted as concentration (evaporation) of lake water dissolved ions (Stevens et al. 2006) are more likely inherited from weathering of the underlying gypsum-bearing sandstones, as an evaporation signal does not register in the lake carbonate $\delta^{18}O$. These revised climatic interpretations are consistent with the KT-3 record (Fig. 10), and with developing research concerning responsiveness of biomes to postglacial climate change (Djamali et al., 2010) and human impacts on Neolithic vegetation management (Roberts 2002) and developing agriculture, all of which can influence pollen-based palaeo-vegetation records (cf. Djamali et al., 2009; Sharifi et al., 2015).

7. Conclusions

Stalagmite KT-3 from Katalekhor Cave in the Zagros Mountains grew through most of the Holocene and its isotopic records are key in better understanding Holocene climate change in the central Zagros region, representative of montane 'fertile crescent' environments, and allowing confident linkage with palaeoclimate records in the Levant, and the monsoonal Arabian Sea region to the SE. Specifically:

1. Stalagmite KT-3 began growing ~9.5 ka under wet early Holocene conditions ($\delta^{18}O$ values around or below -9.0‰, maximum growth diameter and lowest $^{234}U/^{238}U_0$ activity values). Progressive reduction in winter precipitation amount after 7.0 ka is driven by decreasing summer insolation and is expressed by increasing $\delta^{18}O$ and $^{234}U/^{238}U_0$ activity values and reduction in growth diameter until ~2.0 ka. Centennial-scale variability is not a feature of the $\delta^{18}O$ record, Katalekhor being located in an area of stable winter recharge where interannual rainfall variability was probably not marked.

2. KT-3 $\delta^{13}C$ values broadly decrease from ~-2.8‰ to ~-4.0‰ between 9.5 and 4.4 ka, but do show ~ 1.5‰ centennial scale variability with higher $\delta^{13}C$ (<1.5‰) values between 8.3-7.7 ka, 6.5-5.5 ka, 5.4-4.5 ka and ~4.3-2.0 ka. KT-3 $\delta^{13}C$ compositions are enriched relative to lower altitude stalagmites in the Levant, which results from low soil CO_2 contribution and stronger ingress of atmospheric CO_2. Centennial-scale variability is probably thus controlled by small changes in soil development in this case linked to periodic dryness.

3. Three of the centennial-scale dry periods seen in KT-3 $\delta^{13}C$ correspond with Rapid Climate Change (RCC) events based on non-seasalt potassium (K^+) in Greenland ice cores (Mayewski et al., 2004). The first of these, between 8.3-7.7 ka in KT-3, is complicated by overlap with the ~160 year-long, 8.2 ka cold/dry event; however, its culmination corresponds with other regional records that suggest an intensified Siberian High Pressure system affecting Mediterranean regional climate. A broad reversal in KT-3 $\delta^{13}C$ beginning around 4.3 ka and ending soon after 2.0 ka implies sustained aridity that corresponds with a RCC event between 3.5-2.5 ka and the 2.65 to 2.50 ka 'Assyrian megadrought' evident in stable isotope records from Kuna Bar cave in Iraq (Sinha et al., 2019).

4. The KT-3 $\delta^{18}O$ record suggests that nearby lacustrine carbonate isotope records (Lakes Zeribar and Mirabad) can be reinterpreted broadly as insolation-driven records, starting wet, but with recharge decreasing until ~7.0 ka, followed by developing aridity that increased both $\delta^{18}O$ and $\delta^{13}C$.

Acknowledgements

JEA, PJR and SA-O were supported by NERC grant NE/B502944/1; the work was extended by SAC (University of Oxford) through a Leverhulme Trust, Research Project Grant (RPG-2013-235) and by EP in receipt of a NERC studentship through grants NE/L50158X/1 and NE/K500896/1. We very are grateful to Dr Ezzat Raeisi and Dr Naser Asadi (Department of Earth Sciences, College of Sciences, Shiraz University) who provided logistical and practical assistance in support of the fieldwork. Graham Chilvers (UEA) ran the LA-ICPMS and assisted with data reduction, Alan Kendall gave thoughtful discussion of the petrography and Mojgan Soleimani (Innsbruck) provided useful Iranian geological literature. Data reported in this paper are archived at NCDC (https://www.ncdc.noaa.gov/data-access/paleoclimatology-data/datasets/speleothem).

References

Affolter, S., Häuselmann, A., Fleitmann, D., Edwards, R.L., Cheng, H., Leuenberger, M. 2019. Central Europe temperature constrained by speleothem fluid inclusion water isotopes over the past 14,000 years. Science Advances, 5, 9pp, eaav3809.

Ahmadzade, M. and Elmizadeh (2014) Geomorphological evolution of Karst Cave in katalekhor. In 32nd geological Survey of Iran, Tehran, Iran, 15-18 Februrary 2014.

Alley, R.B., Mayewski, P.A., Sowers, T., Stuiver, M., Taylor, K.C. and Clark, P.U., 1997. Holocene climatic instability: a prominent, widespread event 8200 yr ago: Geology, 25, 483-486.

Alley, R.B. and Ágústsdóttir, A.M., 2005. The 8K event: cause and consequences of a major Holocene abrupt climate change: Quaternary Science Reviews, 24, 1123-1149.

Almogi-Labin, A., Bar-Matthews, M., Shriki, D., Kolosovsky, E., Paterne, M., Schilman, B., Ayalon,A., Aizenshtat, Z. and Matthews, A. 2009. Climatic variability during the last ~90ka of the southern and northern Levantine Basin as evident from marine records and speleothems. Quaternary Science Reviews, 28, 2882–2896.

Arshadi, S. and Laumanns, M . 2004. Speleological project Ghar Katalehkhor, pp. 1617-8572. ISSN19

Arz, H. W., Lamy, F., Pätzold, J., Muller, P. J. and Prins, M. 2003. Mediterranean moisture source for an early-Holocene humid period in the northern Red Sea. Science, 300, 118–121.

Barber, D.C., Dyke, A., Hillaire-Marcel, C., Jennings, A.E., Andrews, J.T., Kerwin, M.W., Bilodeau, G., McNeely, R., Southon, J., Morehead, M.D. and Gagnon, J.-M. 1999. Forcing of the cold event of 8,200 years ago by catastrophic drainage of Laurentide lakes. Nature, 400, 344-348.

Bar-Matthews, M., Ayalon, A. and Kaufman, A. 1997. Late Quaternary paleoclimate in the eastern Mediterranean region from stable isotope analysis of speleothems at Soreq Cave, Israel. Quaternary Research, 168, 155–168.

Bar-Matthews, M., Ayalon, A., Kaufman, A. and Wasserburg, G. J. 1999. The Eastern Mediterranean paleoclimate as a reflection of regional events: Soreq cave, Israel. Earth and Planetary Science Letters, 166, 85–95.

Bar-Matthews, M., Ayalon, A., Gilmour, M., Matthews, A. and Hawkesworth, C. J. 2003. Sea–land oxygen isotopic relationships from planktonic foraminifera and speleothems in the Eastern Mediterranean region and their implication for paleorainfall during interglacial intervals. Geochimica et Cosmochimica Acta, 67, 3181–3199.

Bar-Matthews, M. and Ayalon, A. 2011. Mid-Holocene climate variations revealed by high resolution speleothem records from Soreq Cave, Israel and their correlation with cultural changes. The Holocene, 21, 163–171.

Bar-Matthews, M., Keinan, J. and Ayalon, A. 2019 Hydro-climate research of the late quaternary of the Eastern Mediterranean-Levant region based on speleothems research – A review. Quaternary Science Reviews, **221**, 105872.

Barnett, T.P., Dumenil, L., Schlese, U., Roeckner, E., 1988. The effect of Eurasian snow cover on global climate. Science 239, 504–507.

Berberian, M. (1974) A brief geological description of north-central Iran. Geological Survey of Iran Report 29, 127-138.

Borsato, A., Frisia, S., Fairchild, I. J., Somogyi, A. and Susini, J. 2007. Trace element distribution in annual stalagmite laminae mapped by micrometer-resolution X-ray fluorescence: Implications for incorporation of environmentally significant species. Geochimica et Cosmochimica Acta, 71, 1494–1512.

Bowen G. J. and Wilkinson B. 2002. Spatial distribution of $\delta^{18}O$ in meteoric precipitation. Geology 30, 315-318.

Bowen G. J. and Revenaugh J., 2003. Interpolating the isotopic composition of modern meteoric precipitation. Water Resources Research 39, 1299.

Bronk Ramsey C (2008) Deposition models for chronological records. Quat Sci Rev 27: 42–60.

Bronk Ramsey C, Lee S (2013) Recent and planned developments of the program OxCal. Radiocarbon 55:720–730.

Burstyn, Y., Martrat, B., Lopez, J.F., Iriarte, E., Jacobson, M.J., Lone, M.A., Deininger, M., 2019. Speleothems from the Middle East: An Example of Water Limited Environments in the SISAL Database. Quaternary 2, 16.

Carolin, S.A., Walker, R.T., Day, C.C., Ersek, V., Sloan, R.A., Dee, M.W., Talebian, M., and Henderson. G.M., 2019. Precise timing of abrupt increase in dust activity in the Middle East coincident with 4.2 ka social change. Proceedings of the National Academey of Science 116, 67-72.

Cheng, H., Fleitmann, D., Edwards, R.L., Wang, X., Cruz, F.W., Auler, A.S., Mangini, A., Wang, Y, Kong, X., Burns, S.J, and Matter, A. 2009. Timing and structure of the 8.2 kyr B.P. event inferred from δ18O records of stalagmites from China, Oman, and Brazil. Geology, 37, 1007-1010.

Cheng, H., Lawrence Edwards, R., Shen, C.-C., Polyak, V.J., Asmerom, Y., Woodhead, J., Hellstrom, J., Wang, Y., Kong, X., Spötl, C., Wang, X., Calvin Alexander, E., 2013. Improvements in 230Th dating, 230Th and 234U half-life values, and U–Th isotopic measurements by multi-collector inductively coupled plasma mass spectrometry. Earth and Planetary Science Letters 371–372, 82–91.

Cheng, H., Shina, A., Verheyden, S., Nader, F.H., Li, X.L., Zhang, P. Z., Yin, J.J., Yi, L., Peng, Y.B., Rao, Z.G., Ning, Y.F., Edwards, R. L., 2015. The climate variability in northern Levant over the past 20,000 years. Geophysical Research Letters, 42, 8641-8650.

Cheng, H., Spötl, C., Breitenbach, S.F.M., Sinha, A., Wassenburg, J.A., Jochum, K.P., Scholz, D., , Li, X., Yi, L., Peng, Y., Lv, Y., Zhang, P., Votintseva, A., Loginov, V., Ning, Y., Kathayat, G.,Edwards, R. L., 2016. Climate variations of Central Asia on orbital to millennial timescales. Sci. Rep. 6, 36975.

Clarke, G.K.C., Leverington, D.W., Teller, J.T., and Dyke, A.S., 2004. Paleohydraulics of the last outburst flood from glacial Lake Agassiz and the 8200 BP cold event. Quaternary Science Reviews, 23, 389-407.

Copernicus Climate Change Service (C3S) (2017): ERA5: Fifth generation of ECMWF atmospheric reanalyses of the global climate. Copernicus Climate Change Service Climate Data Store (CDS), 2019. https://cds.climate.copernicus.eu/cdsapp#!/home. Neither the European Commission nor ECMWF is responsible for any use that may be made of the Copernicus Information or Data it contains.

Craig, H. 1961. Isotopic variations in meteoric waters. Science, 133, 1702.

Daëron, M., Drysdale, R.M., Peral, M., Huyghe, D., Blamart, D., Coplen, T.B., Lartaud, F., Zanchetta, G., 2019. Most Earth-surface calcites precipitate out of isotopic equilibrium. Nature Communications 10, 429.

Dahl-Jensen, D., Gundestrup, N.S., Miller, H., Watanabe, O., Johnsen, S.J., Steffensen, J.P., Clausen, H.B., Svensson, A., Larsen, L.B., 2002. The NorthGRIP deep drilling programme. Annals of Glaciology 35, 1–4.

Dinpashoh, Y., Fakheri-Fard, A, Moghaddam, M., Jahanbakhsh, S. and Mirnia, M. 2004. Selection of variables for the purpose of regionalization of Iran's precipitation climate using multivariate methods. Journal of Hydrology, **297**, 109–123.

Djamali, M., Beaulieu, J.-L., Miller, N.F., Andrieu-Ponel, V., Ponel, P., Lak, R., Sadeddin, N., Akhani, H., Fazeli, H., 2009. Vegetation history of the SE section of the Zagros Mountains during the last five millennia: a pollen record from the Maharlou Lake, Fars Province, Iran. Veg. Hist. Archaeobot. 18, 123e136. http://dx.doi.org/10.1007/s00334-008-0178-2.

Djamali, M., Akhani, H., Andrieu-Ponel, V., Braconnot, P., Brewer, S., de Beaulieu, J.-L., Fleitmann, D., Fleury, J., Gasse, F., Guibal, F., Jackson, S.T., Lezine, A.-M., Medail, F., Ponel, P., Roberts, N., Stevens, L., 2010. Indian summer monsoon variations could have affected the early-Holocene woodland expansion in the Near East. Holocene 20, 813e820.

Dermody, B. J., de Boer, H. J., Bierkens, M. F. P., Weber, S. L., Wassen, M. J. and Dekker S. C. 2012 A seesaw in Mediterranean precipitation during the Roman Period linked to millennial-scale changes in the North Atlantic Climates of the Past, 8, 637–651.

Eastwood, W., Leng, M., Roberts, N. and Davis, B. 2007. Holocene climate change in the eastern Mediterranean region: a comparison of stable isotope and pollen data from Lake Gölhisar, southwest Turkey. Journal of Quaternary Research, 22, 327–341.

Ebrahimi, B. and Sif, A. (2016) Equilibrium-Line Altitudes of Late Quaternary Glaciers in the Zardkuh Mountain, Iran. Geopersia, 6, 299-322.

Edwards L. R, Chen JH, Wasserburg GJ (1987) 238U-234U-230Th-232Th systematics and the precise measurement of time over the past 500,000 years. Earth and Planetary Science Letters, 81, 175–192.

Ellison, C., Chapman, M., and Hall, I. (2006) Surface and deep ocean interactions during the cold climate event 8200 years ago. Science, 312, 1929-1932.

Elsig, J., Schmitt, J., Leuenberger, D., Schneider, R., Eyer, M.., Leuenberger, M., Joos, J., Fischer, H., and Stocker, T.F. 2009. Stable isotope constraints on Holocene carbon cycle changes from an Antarctic ice core. Nature, 461, 507-510.

Emeis, K.-C., Struck, U., Schulz, H.-M., Rosenberg, R., Bernasconi, S., Erlenkeuser, H., Sakamoto, T. and Martinez-Ruiz, F. 2000. Temperature and salinity variations of Mediterranean Sea surface waters over the last 16, 000 years from records of planktonic stable oxygen isotopes and alkenone unsaturation ratios. Palaeogeography, Palaeoclimatology Palaeoecology, 158, 259–280.

Evans, J. P., Smith, R. B. and Oglesby, R. J. 2004. Middle East climate simulation and dominant precipitation processes. International Journal of Climatology, 24, pp. 1671–1694.

Evans, J.P. and Smith, R.B. 2006. Water vapor transport and the production of precipitation in the eastern Fertile Crescent. Journal of Hydrometeorology, 7, 1295-1307.

Fairchild, I.J., Borsato, A., Tooth, A.F., Frisia, S., Hawkesworth, C.J., Huang, Y., McDermott, F. and Spiro, B., 2000. Controls on trace element (Sr–Mg) composition of carbonate cave waters: implications for speleothem climatic records. Chemical Geology, **166**, 255–269.

Fairchild I. J., Spotl C., Frisia S., Borsato A., Susini J., Wynn P.W. and Cauzid J., 2010. Petrology and geochemistry of annually laminated stalagmites from an Alpine cave (Obir, Austria): seasonal cave physiology. Geol. Soc. Lond. Spec. Publ., 336, 295–321.

Fallah, B., Sodoudi, S., Russo, E., Kirchner, I. and Cubasch, U. 2015. Towards modeling the regional rainfall changes over Iran due to the climate forcing of the past 6000 years. Quaternary International.

Fleitmann, D., Burns, S.J., Mangini, A., Mudelsee, M., Kramers, J., Villa, I., Neff, U., Al-Subbary, A.A., Buettner, A., Hippler, D., Matter, A., 2007. Holocene ITCZ and Indian monsoon dynamics recorded in stalagmites from Oman and Yemen (Socotra). Quaternary Science Reviews 26, 170–188.

Fletcher, W. J. and Sánchez Goñi, M. F. 2008. Orbital- and sub-orbital-scale climate impacts on vegetation of the western Mediterranean basin over the last 48,000 yr. Quaternary Research, 70, 451–464.

Flohr, P., Fleitmann, D., Zorita, E., Sadekov, A., Cheng, H., Bosomworth, M., Edwards, L., Matthews, W., and Matthews, R. 2017. Late Holocene droughts in the Fertile Crescent recorded in a speleothem from northern Iraq, Geophys. Res. Lett., 44,1528–1536.

Frisia, S., Borsato, A., Fairchild, I. J. and Dermott, F. M. C. 2000. Calcite fabrics, growth mechanisms, and environments of formation in speleothems from the Italian Alps and south western Ireland. Journal of Sedimentary Research, 70, 1183–1196.

Frisia, S. and Borsato, A. 2010. Karst. Chapter 6 in Carbonates in Continental Settings: Facies, Environments, and Processes, A.M. Alonso-Zarza and L.H. Tanner (eds.,). Developments in Sedimentology 61, pp. 269–318.

Frisia, S. 2015. Microstratigraphic logging of calcite fabrics in speleothems as tool for palaeoclimate studies. International Journal of Speleology, 44, 1–16. doi:10.5038/1827-806X.44.1.1.

Frumkin, A., Schwarcz, H. P. and Ford, D. C. 1994. Evidence for isotopic equilibrium in stalagmites from caves in a dry region: Jerusalem, Israel. Israel Journal of Earth Sciences 43, 221–230.

Frumkin, A., Ford, D. and Schwarcz, H. 1999. Continental oxygen isotopic record of the last 170,000 years in Jerusalem. Quaternary Research. 327, 317–327. doi:10.1006/qres.1998.2031.

Gat, J. R. and Carmi, I. 1970. Evolution of the isotopic composition of atmospheric waters in the Mediterranean Sea area. Journal of Geophysical Research 75, 3039.

Genty, D., Blamart, D., Ouahdi, R., Gilmour, M., Baker, a, Jouzel, J. and Van-Exter, S. 2003. Precise dating of Dansgaard-Oeschger climate oscillations in western Europe from stalagmite data. Nature, 421, 833–7.

Grant, K.M., Rohling, E.J., Bar-Matthews, M., Ayalon, A., Medina-Elizalde, M., Ramsey, C.B., Satow, C., Roberts, A.P., 2012. Rapid coupling between ice volume and polar temperature over the past 150,000 years. Nature 491, 744–747.

Griffiths, H. I., Schwalb, a. and Stevens, L. R. 2001. Environmental change in southwestern Iran: the Holocene ostracod fauna of Lake Mirabad. The Holocene, 11, 757–764.

Heydarizad, M., Raeisi, E., Sori, R and Gimeno, L. 2018. The identification of Iran’s moisture sources using a Lagrangian particle dispersion model. *Atmosphere*, **9**, 408.

Heydarizad, M., Raeisi, E., Sori, R and Gimeno, L. 2019. Developing meteoric water lines for Iran based on air masses and moisture sources. *Water*, **11**, 2359.

Johnsen, S.J., Clausen, H.B., Dansgaard, W., Gundestrup, N.S., Hammer, C.U., Andersen, U., Andersen, K.K., Hvidberg, C.S., Dahl-Jensen, D., Steffensen, J.P., Shoji, H., Sveinbjörnsdóttir, Á.E., White, J., Jouzel, J., Fisher, D., 1997. The δ 18 O record along the Greenland Ice Core Project deep ice core and the problem of possible Eemian climatic instability. Journal of Geophysical Research: Oceans 102, 26397–26410.

Jones, M.D., Benkaddour, A., Eastwood, W.J., Filippi, M.L., Frogley, M.R., Lamb, H.F., Stein, M., Stevens, L., Valero-Garces, B., Zanchetta, G., 2008. Stable isotope records of Late Quaternary climate and hydrology from Mediterranean lakes: the ISOMED synthesis. Quaternary Science Reviews 27, 2426-2441.

Jones, M. D., Djamali, M., Holmes, J., Weeks, L., Leng, M. J., Lashkari, A., Alamdari, K., Noorollahi, D., Thomas, L. and Metcalfe, S. E., 2015. Human impact on the hydroenvironment of Lake Parishan, SW Iran, through the late-Holocene. The Holocene 25, 1651–1661.

Kaniewski, D., Marriner, N., Cheddadi, R., Morhange, C., Bretschneider, J., Jans, G., Otto, T., Luce, F., and Van Campo, E., 2019. Cold and dry outbreaks in the eastern Mediterranean 3200 years ago. Geology 47, 933–937.

Karevan, M., Vaziri-Moghaddam, H., Mahboubi, A. and Moussavi-Harami, R. 2014 Biostratigraphy and paleo-ecological reconstruction on Scleractinian reef corals of Rupelian-Chattian succession (Qom Formation) in northeast of Delijan area. JGeope 4, 11-14.

Karimi Vardanjani, K., Bahadorinia, S. and Ford, D.C. 2017. An Introduction to Hypogene Karst Regions and Caves of Iran. Chapter 29. In Klimchouk et al., (eds) Hypogene Karst Regions and Caves of the World, Cave and Karst Systems of the World, p. 479-494.

Kaufman, A., Wasserburg, G., Porcelli, D., Bar-Matthews, M., Ayalon, A. and Halicz, L. 1998. U-Th isotope systematics from the Soreq cave, Israel and climatic correlations. Earth and Planetary Science Letters, 156, 141–155.

Kaufmann, G. 2003. Stalagmite growth and palaeo-climate: the numerical perspective. Earth and Planetary Science Letters, 214, 251–266.

Kendall, A.C. and Broughton, P.L., 1978. Origin of fabric in speleothems of columnar calcite crystals. Journal of Sedimentary Petrology 48, 550-552.

Khalili, A. and Rahimi, J. 2014 High-resolution spatiotemporal distribution of precipitation in Iran: a comparative study with three global-precipitation datasets. *Theoretical and Applied Climatology*, **118**, 211–221.

Kisi, O and Shiri, J. 2014. Prediction of long-term monthly air temperature using geographical inputs. International Journal of Climatology, 34, 179–186.

Kutzbach, J.E., Chen, G., Cheng, H., Edwards, R.L. and Liu, Z. 2014. Potential role of winter rainfall in explaining increased moisture in the Mediterranean and Middle East during periods of maximum orbitally-forced insolation seasonality. Climate Dynamics, 42, 1079-1095.

Lambeck, K. 1996. Shoreline reconstructions for the Persian Gulf since the last glacial maximum. Earth and Planetary Science Letters, 142, 43-57.

Leng, M.J., Roberts, N., Reed, J.M., Sloane, H.J. 1999. Late Quaternary palaeohydrology of the Konya Basin, Turkey, based on isotope studies of modern hydrology and lacustrine carbonates. Journal of Paleolimnology, 22, 187–204.

Marino, G., Rohling, E. J., Sangiorgi, F., Hayes, A., Casford, J.L., Lotter, A.F., Kucera, M., Brinkhuis, H. 2009. Early and middle Holocene in the Aegean Sea: interplay between high and low latitude climate variability. Quaternary Science Reviews, 28, 3246-3262.

Mayewski, P.A., Meeker, L.D., Twickler, M.S., Whitlow, S., Yang, Q., Lyons, W.B., Prentice, M., 1997. Major features and forcing of high-latitude northern hemisphere atmospheric circulation using a 110,000-year-long glaciochemical series. Journal of Geophysical Research: Oceans 102, 26345–26366.

Mayewski, P.A., Rohling, E.E., Stager, J.C., Karlen, W., Maasch, K.A., Meeker, L.D., Meyerson, E.A., Gasse, F., van Kreveld, S., Holmgren, K., Lee-Thorp, J., Rosqvist, G., Rack, F., Staubwasser, M., Schneider, R.R., Steig, E.J., 2004. Holocene climate variability. Quaternay Research 62, 243-255.

McDermott, F. 2004. Palaeo-climate reconstruction from stable isotope variations in speleothems: a review. Quaternary Science Reviews, 23, 901–918.

McDonald, J., Drysdale, R., Hill, D., Chisari, R. and Wong, H. 2007. The hydrochemical response of cave drip waters to sub-annual and inter-annual climate variability, Wombeyan Caves, SE Australia. Chemical Geology, 244, 605–623.

Mehterian, S., Pourmand, A., Shari, A., Lahijani, H. A. K., Naderi, M. and Swart, P. K. (2017). Speleothem records of glacial/ interglacial climate from Iran forewarn of future water availability in the interior of the Middle East. Quaternary Science Reviews, 164, 187–198.

Miller, G., Mangan, J., Pollard, D., Thompson, S., Felzer, B. and Magee, J. 2005. Sensitivity of the Australian Monsoon to insolation and vegetation: Implications for human impact on continental moisture balance. Geology, 33, 65-68.

Modarres, R. and Sarhadi, A. 2011. Statistically-based regionalization of rainfall climates of Iran. Global and Planetary Change. 75, 67–75.

Peckover, E.N., Andrews, J.E., Leeder, M.R., Rowe, P.J., Marca, A., Sahy, D., Noble, S., and Gawthorpe, R.L., 2019. Coupled stalagmite – alluvial fan response to the 8.2 ka event and early Holocene palaeoclimate change in Greece. *Palaeogeography, Palaeoclimatology, Palaeoecology* **532,** 109252.

Rasmussen, S.O., Andersen, K.K., Svensson, A.M., Steffensen, J.P., Vinther, B.M., Clausen, H.B., Siggaard-Andersen, M.-L., Johnsen, S.J., Larsen, L.B., Dahl-Jensen, D., Bigler, M., Röthlisberger, R., Fischer, H., Goto-Azuma, K., Hansson, M.E., Ruth, U., 2006. A new Greenland ice core chronology for the last glacial termination. Journal of Geophysical Research 111.

Raziei, T., Mofidi, A., Santos, J.A., Bordi, I. 2012. Spatial patterns and regimes of daily precipitation in Iran in relation to large-scale atmospheric circulation. International Journal of Climatology, 32, 1266-1237.

Raziei, T., Bordi, I., Santos, J.A. and Mofidi, A. 2013. Atmospheric circulation types and winter daily precipitation in Iran. International Journal of Climatology, 33, 2232–2246.

Raziei, T., Daryabari, J. and Bordi, I. 2014. Spatial patterns and temporal trends of precipitation in Iran. *Theoretical and Applied Climatology*, **115**, 531–540.

Roberts, N., Reed, J.M., Leng, M.J., Kuzucuoğlu, C., Fontugne, M., Bertaux, J., Woldring, H., Bottema, S., Black, S., Hunt, E. and Karabiyikoğlu, M. 2001. The tempo of Holocene climatic change in the eastern Mediterranean region: new high-resolution crater-lake sediment data from central Turkey. The Holocene, 11, 721-736

Roberts, N., 2002. Did prehistoric landscape management retard the post-glacial spread of woodland in Southwest Asia? Antiquity 76, 1002-1010.

Roberts, N., Jones, M.D., Benkaddour, A., Eastwood, W.J., Filippi, M.L., Frogley, M.R., Lamb, H.F., Leng, M.J., Reed, J.M., Stein, M., Stevens, L., Valero-Garces, B., Zanchetta, G., 2008. Stable isotope records of Late Quaternary climate and hydrology from Mediterranean lakes: the ISOMED synthesis. Quaternary Science Reviews 27, 2426-2441.

Robinson L.F., Belshaw N.S., Henderson G.M. 2004. U and Th concentrations and isotope ratios in modern carbonates and waters from the Bahamas. Geochimica et Cosmochimica Acta, 68, 1777–1789.

Robinson, S. A., Black, S., Sellwood, B. W. and Valdes, P. J. 2006. A review of palaeoclimates and palaeoenvironments in the Levant and Eastern Mediterranean from 25,000 to 5000 years BP: setting the environmental background for the evolution of human civilisation. Quaternary Science Reviews, 25, 1517–1541. doi:

Rohling, E.J., Mayewski, P.A., Hayes, A., Abu-Zied, R.H., Casford, J.S.L., 2002. Holocene atmosphere–ocean interactions: records from Greenland and the Aegean Sea. Climate Dynamics 18, 587–593.

Rohling, E.J., Pälike, H., 2005. Centennial-scale climate cooling with a sudden cold event around 8,200 years ago. Nature 434, 975–979.

Rohling, E. J, Marino, G., Grant, K.M., Mayewski, P.A., Weninger, B. 2019. A model for archaeologically relevant Holocene climate impacts in the Aegean-Levantine region (easternmost Mediterranean). Quaternary Science Reviews, 208, 38-53.

Rowe, P. J., Mason, J. E., Andrews, J. E., Marca, A. D., Thomas, L., van Calsteren, P., Jex, C. N., Vonhof, H. B. and Al-Omari, S. 2012. Speleothem isotopic evidence of winter rainfall variability in northeast Turkey between 77 and 6 ka. Quaternary Science Reviews, 45,60–72.

Rowe, P. J., Wickens, L.B., Sahy, D., Marca, A.D., Peckover, E., Noble, S., Özkul, M., Baykara, M.O. Millar, I.L and Andrews, J. E. 2020. Multi-proxy speleothem record of climate instability during the early last interglacial in southern Turkey. Palaeogeography, Palaeoclimatology, Palaeoecology, 538, 109422.

Rozanski, K., Araguas-Araguas, L. and Gonfiantini, R. 1993. Isotopic patterns in modern global precipitation. In: Climate Change in Continental Isotopic Records (Ed. by P.K. Swart, K.C. Lohmann, J. McKenzie and S. Savin), 1-36. Geophysical Monograph 78. American Geophysical Union, Washington, DC.

Rutlidge, H., Baker, A., Marjo, C. E., Andersen, M. S., Graham, P. W., Cuthbert, M. O., Rau, G. C., Roshan, H., Markowska, M., Mariethoz, G. and Jex, C. N. 2014. Dripwater organic matter and trace element geochemistry in a semi-arid karst environment: Implications for speleothem paleoclimatology. Geochimica et Cosmochimica Acta, 135, 217–230.

Sardarabadi, S., Jahani, D. and Ghadimvand, N.K. (2016) Facies, Depositional Environment and Diagenesis of the Qom Formation in Rameh Section (Northeastern Garmsar). Open Journal of Geology, 6, 1240-1256.

Schmidt, A., Quigley, M., Fattahi, M., Azizi, G., Maghsoudi, M. and Fazeli, H. 2011. Holocene settlement shifts and palaeoenvironments on the Central Iranian Plateau: Investigating linked systems. The Holocene, 21, 583–595.

Shamsi, A. and Kazemi, G. A. 2014. A review of research dealing with isotope hydrology in Iran and the first Iranian meteoric water line. Geopersia, 4, 73–86.

Sharifi, A., Pourmand, A., Canuel, E. A., Ferer-Tyler, E., Peterson, L. C., Aichner, B., Feakins, S. J., Daryaee, T., Djamali, M., Beni, A. N., Lahijani, H. A. K. and Swart, P. K. (2015) “Abrupt climate variability since the last deglaciation based on a high-resolution, multi-proxy peat record from NW Iran: The hand that rocked the Cradle of Civilization? Quaternary Science Reviews, 123, 215– 230.

Sinha, A., Kathayat, G., Weiss, H., Li, H., Cheng, H., Reuter, J., Schneider, A.W., Berkelhammer, M., Adali, S.F., Stott, L.D., Edwards, R.L. 2019. Role of climate in the rise and fall of the Neo-Assyrian Empire. Science Advances 5, eaax6656.

Stevens, L., Wright, H. and Ito, E. 2001. Proposed changes in seasonality of climate during the Lateglacial and Holocene at Lake Zeribar, Iran. The Holocene, 11, 747–755.

Stevens, L. R., Ito, E., Schwalb, A. and Wright, H. E. 2006. Timing of atmospheric precipitation in the Zagros Mountains inferred from a multi-proxy record from Lake Mirabad, Iran. Quaternary Research, 66, 494–500.

Stewart, M. K. 1975. Stable isotope fractionation due to evaporation and isotopic exchange of falling waterdrops: applications to atmospheric processes and evaporation of lakes. Journal of Geophysical Research, 80, 1133–1146.

Sun, Q., Liua, Y., Salem, A., Marks, L., Welc, F., Ma, F., Zhang, W., Chen, J., Jianga, J., Chen, Z. 2019. Climate-induced discharge variations of the Nile during the Holocene:

Evidence from the sediment provenance of Faiyum Basin, north Egypt. Global and Planetary Change, 172, 200–210.

Tremaine, D. M., Froelich, P. N. and Wang, Y, 2011. Speleothem calcite farmed *in situ*: Modern calibration of $\delta^{18}O$ and $\delta^{13}C$ palaeoclimate proxies in a continuously-monitored natural cave system. Geochimica et Cosmochimica Acta, 75, 4929-4950.

Tremaine D. M. and Froelich P. N., 2013. Speleothem trace element signatures: a hydrological geochemical study of modern cave dripwaters and farmed calcite. Geochimica et Cosmochimica Acta, 121, 522-545.

Ulbrich, U., Lionello, P., Belušic´, D., Jacobeit, J., Knippertz, P., Kuglitsch, F.G., Leckebusch, G.C., Luterbacher, J., Maugeri, M., Maheras, P., Nissen, K.M., Pavan, V., Pinto, J.G., Saaroni, H., Seubert, S., Toreti, A., Xoplaki, E., Ziv, B., 2012. Climate of the Mediterranean: Synoptic Patterns, Temperature, Precipitation, Winds, and their Extremes. In: P.Lionello (ed.): The Climate of the Mediterranean Region, From the past to the future, *Elsevier, Dordrecht*, ISBN: 9780124160422, 301-346.

Vaks, A., Gutareva, O. S., Breitenbach, S. F. M., Avirmed, E., Mason, A. J., Thomas, A. L., Osinzev, A.V, Kononov, A. M. and Henderson, G. M. 2013. Speleothems reveal 500,000-year history of Siberian permafrost. Science, 340, 183–186.

Van der Horn, S. A., van Kolfschoten, T., van der Plicht, J. and Hoek, W. Z. 2015. The effects of the 8.2 ka event on the natural environment of Tell Sabi Abyad, Syria: Implications for ecosystem resilience studies. *Quaternary International*, **378**, 111–118.

Verheyden, S., Nader, F. H., Cheng, H. J., Edwards, L. R. and Swennen, R. 2008. Paleoclimate reconstruction in the Levant region from the geochemistry of a Holocene stalagmite from the Jeita cave, Lebanon. Quaternary Research, 70, 368–381.

Vinther, B.M., Clausen, H.B., Johnsen, S.J., Rasmussen, S.O., Andersen, K.K., Buchardt, S.L., Dahl-Jensen, D., Seierstad, I.K., Siggaard-Andersen, M.-L., Steffensen, J.P., Svensson, A., Olsen, J., Heinemeier, J., 2006. A synchronized dating of three Greenland ice cores throughout the Holocene. Journal of Geophysical Research 111.

Walker, R. T. and Fattahi, M. 2011. A framework of Holocene and Late Pleistocene environmental change in eastern Iran inferred from the dating of periods of alluvial fan abandonment, river terracing, and lake deposition. Quaternary Science Reviews, 30, 1256–1271.

Wasylikowa, K., Witkowski, A., Walanus, A., Hutorowicz, A., Alexandrowicz, S.W., Langer, J.J. 2006. Palaeolimnology of Lake Zeribar, Iran, and its climatic implications. Quaternary Research, 66, 477-493.

Wick, L., Lemcke, G. and Sturm, M. 2003. Evidence of Lateglacial and Holocene climatic change and human impact in eastern Anatolia: high-resolution pollen, charcoal, isotopic and geochemical records from the laminated sediments of Lake Van, Turkey. The Holocene, 13, 665–675.

Wright, Jr., H.E. (1962) Pleistocene glaciation in Kurdistan. Eiszeialter und Gegenroart, 12, 131-164.

Ye, H.C., Bao, Z.H., 2001. Lagged teleconnections between snow depth in northern Eurasia, rainfall in Southeast Asia and sea-surface temperatures over the tropical Pacific Ocean. International Journal of Climatology 21, 1607–1621.

Zanchetta, G., Drysdale, R. N., Hellstrom, J. C., Fallick, A. E., Isola, I., Gagan, M. K. and Pareschi, M.T. 2007. Enhanced rainfall in the Western Mediterranean during deposition of sapropel S1: stalagmite evidence from Corchia cave (Central Italy). Quaternary Science Reviews, 26, 279–286.